On The Two Stream Instability
In Pulsar Magnetospheres

Maximilian Imgrund

SIGILL · UNIVERSITAT · LUDOVIC · MAXIM

München 2012

On The Two Stream Instability
In Pulsar Magnetospheres

Maximilian Imgrund

Master Thesis
within the Elite Master Program
Theoretical And Mathematical Physics
of Ludwig–Maximilians–Universität
München

handed in by
Maximilian Imgrund
from Lohr am Main

Munich, 7$^{\text{th}}$ of August 2012

Erstgutachter: Prof. H. Ruhl
Zweitgutachter: Prof. H. Lesch

Contents

1. Introduction 3
1.1. Pulsar formation and evolution . . . 4
1.2. Observational picture and outer magnetosphere . . . 6
1.3. Inner magnetosphere and radio emission zone . . . 7
1.4. Radio footprint of a pulsar . . . 9
1.5. Radio Emission Processes . . . 12
1.6. Constraints to be fulfilled . . . 12

2. Analysis of the two stream instability 15
2.1. Derivation of the dispersion relation . . . 15
2.2. Analysis of dispersion relation . . . 17
2.3. Structure formation and limits of application . . . 20
2.4. Numerical measurement . . . 22
2.5. Concluding remarks on the analysis . . . 24
2.6. The nonlinear regime - an outlook . . . 26

3. Damping the TSI 29
3.1. Damping by stretching . . . 29
3.2. Comparison of damping and amplification . . . 31
3.3. Detuning by energy gain . . . 32
3.4. Discussion and numerical verification of the criteria . . . 33
3.5. Application to pulsar model . . . 36

4. Two processes of radio radiation 39
4.1. Radiation by high-gamma background . . . 39
4.2. Self-radiation in nonlinear phase . . . 41
4.3. Coupling of different processes and real radiative output . . . 43

5. Results 45
5.1. What has been done . . . 45
5.2. What should be done . . . 46
5.3. What remains to be said . . . 47

A. Derivations 49
A.1. Brightness temperature approximation . . . 49
A.2. Larmor's formula in terms of an external potential . . . 49

B. Numerical Methods **51**
B.1. The Plasma Simulation Code 51
B.1.1. The Yee algorithm 52
B.1.2. Vlasov equation and the quasiparticle approach 53
B.2. Simbox setup 56
B.2.1. Choosing geometry and boundary conditions 56
B.2.2. Determining and setting initial field and currents 58
B.2.3. Modifying the setup to maintain a quasi constant E_z field . . 60
B.3. Integrating E_z to gain a notion of potential 61

C. Normalization **63**

D. Table of simulations **65**

E. Used tools **67**

Bibliography **69**

Acknowledgments... **73**

Selbstständigkeitserklärung **75**

1. Introduction

> Eine ältere Dame in einem Usedomer Supermarkt nimmt eine ganze Palette von Joghurt mit Tropenfrüchten aus dem Kühlregal und erklärt dem Autor dieser Arbeit:
> "Wissen Sie, ich nehme ja nur die Exoten."

Pulsars are exotic in every aspect of their existence and take physics to yet another extreme. They serve as both test-bed and showcase of lots of fundamental physics like quantum electrodynamics in strong fields[HL06] or general relativity [KW09]. These rapidly rotating objects may e.g. give insights about the still unknown equation of state of the neutron star, the core of the pulsar. Providing high luminosity, precision timings as well as fields exceeding 10^{13} Gauss they are of great interest for a broad range of research topics. Especially the radio emission shows both interesting structure and promising perspective to test fundamental physics. While already being actively used for research, its exact origin remains unknown. Exact identification of the emission process would not only add another cornerstone to the understanding of pulsar magnetospheres but also give the opportunity to gain accuracy in timing models and the assumptions therein.

This thesis analyses one candidate driving process for radio emission, the two stream instability both in terms of analytic calculations and simulations. As will be shown, the TSI is not only strong and fast enough to be a candidate for radio emission but also shows promising scaling behaviour with pulsar parameters as well as the right mixture between existence in all pulsar magnetospheres and being suppressed for most parts of an individual magnetosphere.

A basic knowledge of pulsars, a special category of neutron stars is vital to understand the approximations and assumptions our analysis is based on. Therefore we begin our thesis by reviewing the basic principles of pulsar and neutron star physics, give reasoning on the structure of a pulsar magnetosphere and review the characteristics of radiation output. Concluding our introductory chapter we will give an overview over the various proposed radiation mechanisms.

Thereafter we will carry out a thorough analytical analysis of the TSI instability presenting also numerical results to test both our derivation and the code. Proceeding with analysing the interplay between the fields of a pulsar magnetosphere and the TSI we will derive restrictions to the development of the instability and examine where the TSI arises in a pulsar magnetosphere.

A process proposal would not be complete without at least an estimation on the

power output yielded. We give such a rough calculation in the chapter before concluding the astrophysical part of our thesis by summarizing our results.
In the appendix we have collected a brief introduction to the PSC, the plasma simulation code used, as well as detailed descriptions of our case's setup along with the input data to the simulations presented throughout the thesis. The interested reader will stumble upon some derivations of formulae used in the text.
As outlined, let us begin with the birth of a pulsar, introducing us to the basic pulsar physics.

1.1. Pulsar formation and evolution

The following sections review common knowledge in the field of pulsar astronomy and use arguments partly adapted from [Cam98, Rit93, Kra95].
Pulsars basically are fast rotating neutron stars(which themselves have been proposed by Baade and Zwicky [BZ34] 1934). This type of star may be formed when a main sequence star or a mass accreting white dwarf ends up in a supernova. The basic mechanism is triggered by the depletion of lighter elements in the core and the breakdown of the corresponding fusion processes. This leads to an absence of radiation pressure. Consequently the star further collapses until the temperature and pressure in it reaches the next higher fusion threshold. This goes on until iron is produced, which has the maximum binding energy per nucleon and thus would not set free any energy by fusion processes. This leads to a sudden pressure drop in the core. The hull of the star falls onto the core. Gravitations pressure on the remnants of the core is so heavy that the Fermi pressure on electrons rises to a level where the inverse beta decay of electrons with protons to neutrons and electron neutrinos is favoured. The iron core collapses to pure neutrons now forming a macroscopic atomic nucleus. This happens if the iron core has a mass over the Chandrasekhar limit[Cha83] of about $1.44 M_\odot$. Because of its degenerated state the core is quite inelastic and reflects the incoming shockwaves from the still ongoing collapse. The shock, additionally driven by thermonuclear fusion of the remaining lighter elements, blasts the hull into space. A neutron star consists of degenerate superfluid neutrons and some protons in the core surrounded by a crust of iron with traces of other elements. Since it possesses a density of an atomic nucleus and is formed out of the remains of a normal star, a neutron star is, with a typical radius of about 10km a very compact object. The super nova per se is a quite symmetric process and thus can be assumed to conserve angular momentum. This conservation leads to a speedup of the naturally existing rotation of the star. We may conclude:

$$E_{\mathrm{rot}} = \frac{1}{2} I_{pre} \Omega_{pre}^2 = \frac{1}{2} I_{NS} \Omega_{NS}^2 = I_{NS} \frac{2\pi^2}{P^2} \tag{1.1}$$

$$\frac{\Omega_{NS}}{\Omega_{pre}} \approx \sqrt{\frac{I_{pre}}{I_{NS}}} \approx \frac{r_{pre}}{r_{NS}} \tag{1.2}$$

Where E_{rot} is the rotation energy, $I_{\mathrm{pre/NS}}$ the moment of inertia before and after collapse, Ω the rotation frequency and $P = \frac{2\pi}{\Omega}$ the rotation period and we have used that for the moment of inertia $\int \mathrm{d}V r^2 \rho \approx mr^2$ approximately holds. Thus the collapse leads to a spinup approximately determined by the radii's ratio of star and neutron star. This easily leads to factors of 10^6; typical rotation periods of days for a star become seconds and beyond. There's a lower limit to the period since a neutron star may only rotate as fast as its surface stays below the velocity at which centrifugal surmount gravitational forces. We thus conclude for a period:

$$E_{Rot} \approx \frac{GM_{NS}^2}{r_{NS}} \left(\frac{P_{crit}}{P}\right)^2 \tag{1.3}$$

$$P_{crit} = \pi r_{NS} \sqrt{\frac{r_{NS}}{GM_{NS}}} \approx 0.5ms \text{ for } r_{NS} \approx 12km \tag{1.4}$$

where we've assumed $I_{NS} \approx \frac{1}{2} M_{NS} r_{NS}^2$. Calculating for a neutron star of $1.5M_{\odot}$ at a period of $1s$ and radius of $10km$ we yield the total rotational energy $E_{\mathrm{rot}} = 2.8 \cdot 10^{48} Erg$.

The period is not the only quantity affected by the collapse. Stars generate a magnetic field by the magnetohydrodynamic dynamo mechanism of about 100G. It is an elementary result of basic plasma physics, that, when the plasma is dominating the magnetic field (which is the case for a star as whole) the magnetic field lines are effectively frozen into the plasma and carried away with its movement. This means, large scale change of an magnetic field in this case is coupled to the flow of plasma. We know by Maxwell's equation that the B-field is divergence free. This means by Gauss' theorem:

$$\int_V \mathrm{d}^3x \,\mathrm{div}\vec{B} = \int_{\partial V} \mathrm{d}\vec{A}\vec{B} = 0; \tag{1.5}$$

If we now divide the whole surface of the star into a northern and southern hemisphere, and let the B-field scale with B_0, then this equation simply states that the flux through the northern hemisphere equals the flux through the southern. The integrals are invariant to surface deformation and yield a constant. Now the surface of the star will shrink since it collapses. This does not change topology of the problem in our case, which means that the evolution of the collapse does not affect the flux:

$$\frac{\mathrm{d}}{\mathrm{d}t}\Phi = \frac{\mathrm{d}}{\mathrm{d}t} \int_{\text{hemisphere}} \mathrm{d}\vec{A}\vec{B} = 0 \tag{1.6}$$

by symmetry we conclude that the local flux is also conserved under transformation, and thus

$$B_{0,NS} = B_{0,star} \frac{A_{star}}{A_{NS}} \tag{1.7}$$

which states that a neutron star may be a rotating magnetic dipole of $B_0 = 10^{14} G$. For real pulsars, typical magnetic field strengths are $10^{12} G$ indicating a loss of magnetic flux during formation.

Since the rotational and magnetic axes may not be aligned[1] such a magnetic field of course radiates and by that slows rotation.
We may calculate the loss of energy by observing the spindown, $\dot{P}$, and deriving (1.1) w.r.t. time:

$$\dot{E}_{\mathrm{rot}} = -\frac{4\pi^2 I_{NS}}{P^2}\frac{\dot{P}}{P} \tag{1.8}$$

For typical relative slippages of 10^{-15} we yield an energy loss of tremendous $5.6 \cdot 10^{33} erg/s$ which is about the power output by the sun. Only a small fraction of this energy is converted into radio frequency. Typical total energy outputs are in the range of $10^{30} erg/s < \dot{E}_{\mathrm{rot}} < 4 \cdot 10^{38} erg/s$. Because of the tremendous rotational energies involved, a pulsar can be taken as rigid timing device competing with atomic clocks which are just reaching a relative accuracy of 10^{-15} [NIS06]. However there are rare (w.r.t. time) but common (w.r.t. different pulsars) events of time slips[2] accounted to structural deformation of the iron crust that nearly instantly modify the moment of inertia.
The associated pulsar lifetime in a crude estimate by $\frac{1}{\dot{P}}$ is something like $10^{15}s$, yielding 30 million years. Remaining nebulae created by the expelled hull of a supernova vanish from sight by movement or dilatation after a few 10,000 years leaving the pulsar in our view.

1.2. Observational picture and outer magnetosphere

Spectacular evidence of a young pulsar is the crab nebula. The supernova observed AD 1054 by chinese astronomers[3] created both nebula and the crab pulsar (see fig. 1.1). The nebula's high radiation by gyration of charge carriers around a magnet field of mG strength needs γ-factors of 10^6. The relaxation time for such a process is much shorter than the lifetime of the nebula and thus the relativistic particles have to be constantly supplied by the crab pulsar. The pictures thus show direct evidence of the wind the pulsar drives with its energy dissipation of about $4 \cdot 10^{38} erg/s$ [Cam98]
The wind itself is caused by the rotating magnetic axis. In the case of non-aligned rotation and magnetic axis, the dipole magnetic field has to show a form differing from a dipole at the distance where the distance r from the rotation axis is $\Omega r > c$ since the fields and particles cannot propagate with a speed exceeding the speed of light. The field lines of a dipole field which lie completely within this so called light cylinder roughly follow the classical dipole solution and are closed in the sense that they start and end at the pulsar's surface. The wind is driven by the so called open field lines. They leave the pulsar's surface near the pole to cross the light cylinder , wind up and stretch out until they interact with the ISM[4].

---

[1] parallel alignment is called the case of an aligned rotator

[2] so called glitches

[3] and possibly others

[4] interstellar medium

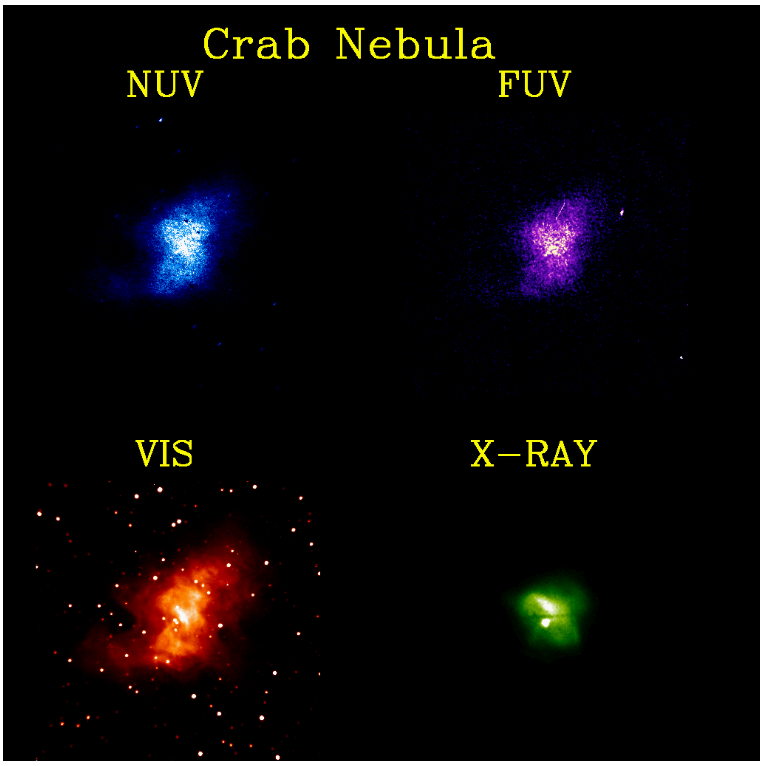

Figure 1.1.: Observational appearance of the crab nebula in optical, UV and γ-rays [NU96] most of the energy output of the crab pulsar drives the emissions of the wind zone.

1.3. Inner magnetosphere and radio emission zone

The relevant area for this thesis however lies a few ten to hundred pulsar radii above the surface of the pulsar and not in the wind zone. There we can model the pulsar magnetosphere to consist of more or less closed field lines and a cone of open field lines over every magnetic pole. This becomes clear since radio emissions are coupled to the rhythm of this cone crossing the line of sight to earth. A pictorial approach to the inner structure is given in fig.1.2. Goldreich and Julian 1969 [GJ69] proposed a model for the structure of the inner magnetosphere. Even though it is a static model and thus expected to break down for the open field lines, observations[KLO$^+$06] suggest that it is not far from the right picture and the Goldreich Julian density is still a fairly good assumption for the plasma density. They take a closed magnetic dipole field as basic assumption in which the neutron star's plasma is rotating. To form a static model, the arising Lorentz force $\propto \vec{v} \times \vec{B}$ has to be balanced by an electric field created by an arising charge density. This charge density is statically hold by the closedness of the field lines restricting its movements to the field's geometry. Putting this into formulae yields [GJ69] (in spherical coordinates and aligned rotator case):

$$\Phi(\theta, r) = -\frac{B_o \Omega r_{NS}^5}{3cr^3} P_2(cos(\theta)) \qquad (1.9)$$

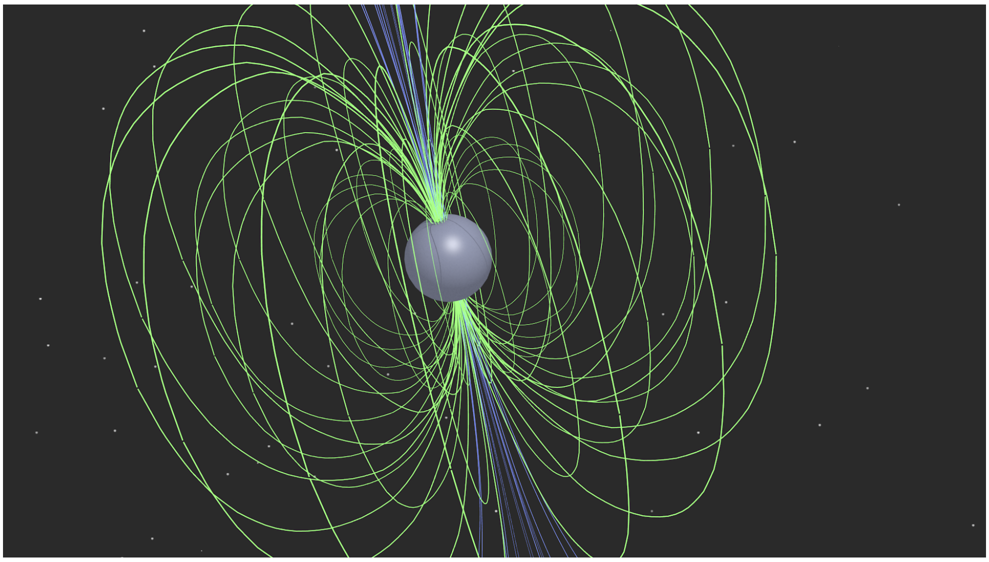

Figure 1.2.: One may imagine the inner zone of a pulsar magnetosphere consisting of closed field lines (depicted green) holding static density of plasma and a region of open field lines (depicted blue) with high electric field gradients driving jets.

Where $P_2(cos(\theta))$ is the second Legendre Polynomial, which for small θ may be set to 1 since it goes like θ^4 around small θ. We use the approximation of an aligned rotator throughout our thesis and expect the preceding to hold. Φ is the electric potential created by the Goldreich Julian charge density,

$$|e \cdot n_{GJ}(r)| = 4\frac{B_o\Omega}{c}\left(\frac{r_{NS}}{r}\right)^5 \tag{1.10}$$

This of course only holds for the closed field line area since charge carriers on open field lines are free to exit the pulsar at the poles. Gravitational forces, as strong they might be are exceeded by electric forces by a factor of

$$\frac{F_{el}}{F_{grav}}\frac{e\frac{B_o\Omega r_{NS}}{3c}}{\frac{GM_{NS}m_e}{r_{NS}^2}} = \frac{eB_o\Omega r_{NS}^3}{3cGM_{NS}m_e} \approx 10^{11} \tag{1.11}$$

for electrons or positrons. At such a ratio, it becomes clear that pulsars may drive strong jets into the surrounding space.

The pulsar magnetosphere's density often is described to be a factor of ζ, the so called multiplicity, more dense than the net charge density derived n_{GJ} suggests. At such high field values it is agreed upon that a pulsar sustains a positron-electron-plasma. However exact pair creation rates are unknown and expected not to have a dramatic cascading behaviour. In this setting, the high fields parallel to the open field lines excite the question of limitation of output flow. Both the emission work on charge carriers from the polar cap region[JLK01] and the limit by space charge effects [JLK02] have been intensively studied and may perhaps lead to an explanation of

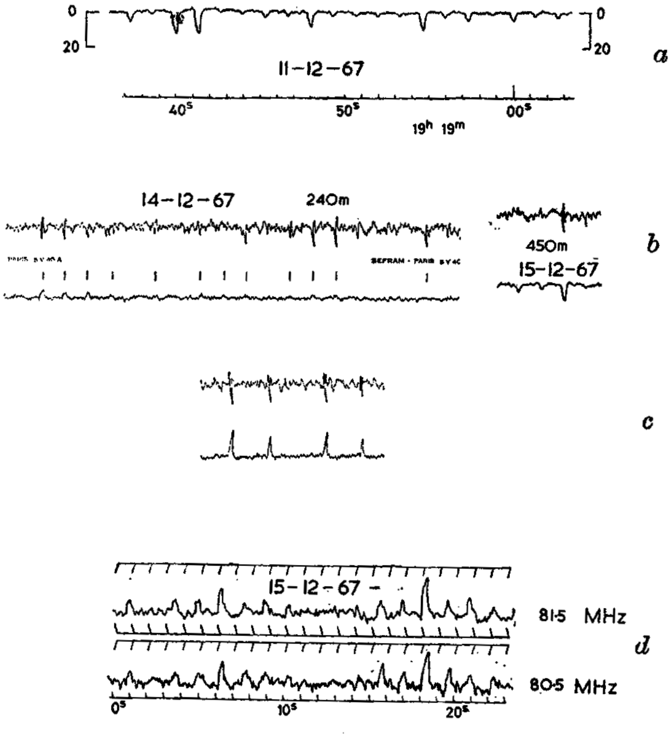

Figure 1.3.: One of the first observations from the paper of Bell and Hewish '68[HBP+68]: *a*, A record of the pulsating radio source in strong signal conditions (receiver time constant $0.1s$). Full scale deflexion corresponds to $20 \cdot 10^{-24} \frac{W}{m^2 Hz}$. *b*, Upper trace records obtained with additional paths ($240m$ and $450m$) in one side of the interferometer. Lower trace: normal interferometer records.(The pulses are small for $l = 240m$ because they occurred near a null in the interference pattern; this modifies the phase but not the amplitude of the oscillatory response on the upper trace.) *c*, Simulated pulses obtained using a signal generator.*d*, Simultaneous reception of pulses using identical receivers tuned to different frequencies. Pulses at the lower frequency are delayed by about $0.2s$.

the typical off-periods a pulsar undergoes. Before we turn to the possible origins of radio radiation, let us describe the typical observational appearance of a pulsar in a radio telescope.

1.4. Radio footprint of a pulsar

What Bell and Hewish[HBP+68] have detected on the 28th of November 1967 was what its later name states: a *puls*ating st*ar*. It was a periodically emitting point of radio radiation in the sky. Fluctuations in radio signals are quite common, since the interstellar medium can cause scintillation[5] that also appear as a point source. Distinguishing noise from a regular occurring signal was not easy at that time, especially when usually a periodical signal meant, that one has caught a terrestrial disturbance. Figure 1.3 shows the signals displayed in the original paper published in Nature. Besides the periodicity, one already may extract another characteristic feature of radio emissions in part b of the figure: A pulsar may interrupt its signal for several periods. This phenomenon was entitled *nulling*. The underlying process

---

[5] scintillation in astrophysics usually means the twinkling of a star by atmospheric disturbances

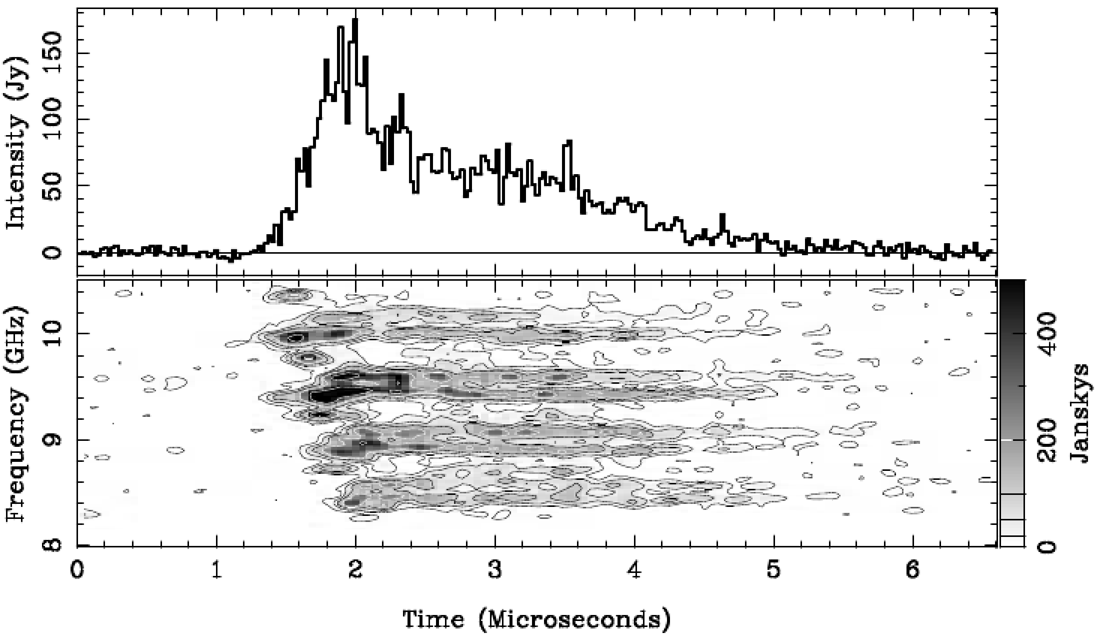

Figure 1.4.: Comb-like frequency structure observed for *ns* to *μs* subpulses. Graphic from [HKWE03]

causing the nulling has to take a timescale comparable to one to several pulsar periods. Observing lots of succeeding periods in detail, one finds another two timescales of variation. A single period is never like the other and consists of lots of seemingly random radiation outbreaks. However averaged over several hundred pulsar periods, every pulsar radiates according to its characteristic fingerprint and is thus distinguishable from other pulsars. The fingerprint may perhaps only change significantly over long time or after period glitches which are expected to correspond to larger changes on the surface of the neutron star. We conclude that the average profile varies on the scale of thousands of pulsar periods. But every pulse itself turns out to consist of nanosecond outbreaks (nanoshots) cumulating to microbursts of radiation in the hundred Mhz to Ghz range[HKWE03]. This holds perhaps not only for some but for all pulsars. Since the timescale is near the wavelength one has to put some effort into reconstructing frequencies out observational data but thorough analysis suggests that these subpulses may have a comb-like structure (see fig. 1.4). Overall radiated energy in the radio range is considerably less than 1/1000 of total output and typically yield absolute values of $10^{28} erg/s$. Concluding from the plot in fig. 1.4 one deduces that luminosities are only weakly dependent on the pulsar parameters. (The broad distribution comes with varying distance to the pulsars since displayed are measured luminosities per area and frequency range). E.g. the mean observed luminosities vary only about one and a half magnitudes w.r.t. B/P which demands the radiation process to be only weakly dependent on B and P alone. A possible radiation process producing such nanoshots is only happening a tiny fraction of the

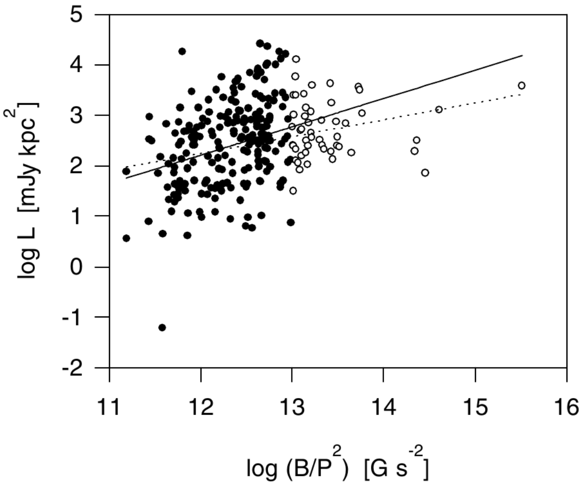

Figure 1.5.: Graphics from [AH00]: Depicted with filled dots are young pulsars. Old pulsars are marked with circles while the dotted line is a fit over the overall population and the normal line is fitted to the old population.

whole time, thus its calculated peak power should be a few magnitudes higher than the overall averaged luminosity perceived. Propagation of this pulse through the magnetosphere furthermore may reduce its radiation power. Consequently a viable candidate process should have a peak power at least two or three orders bigger than $10^{28} erg/s$ to account for the luminosities observed. The ns to μs duration of such a shot also indicates, that the emission region is quite narrow and on the order of centimetres and meters. Could the radio output be simply of thermal origin? One may estimate the brightness temperature of an object by the formula from it's power output in a given narrow frequency band as (a quick derivation is given in A.1):

$$T_{bb} = \frac{c^2 L_\nu}{2\nu^2 \delta\nu A} \approx 10^{29} K \tag{1.12}$$

evaluated for $\nu = 10^8 Hz, \Delta\nu = 10^7 Hz, A = 10^{13} cm^2$.These tremendous temperatures will not be found in a pulsar magnetosphere and consequently incoherent radiation by e.g. thermal radiation is to be excluded. Accordingly the search for an appropriate radio emission process concentrated on coherent processes.

Another phenomenon gaining a lot of attention is the polarization of the received radiation. Since most processes are oriented due to restriction of motion along the field lines, the thus emitted radiation is highly polarized for most of the candidate processes. Travelling through the magnetosphere, both refraction and propagation of each mode implies complex coupling mechanisms. The impact of these in our case secondary processes can therefore not be taken into account. To model a possible signal by the processes described within this thesis, one would have to implement a reasonable calculation to respect propagation. This was left for future investigation. A useful overview over pulse propagation through the magnetosphere can be found in [Gra99].

1.5. Radio Emission Processes

The following section intents to give an overview about emission process candidates found in literature. It abbreviates the considerations given in [Gra99]. The emission processes can be split up into the region they come from and the driving process. At the polar cap, we could expect thermal emissions, however the temperatures involved may perhaps account for the γ-ray fraction, but not the radio part. Thinking first order, the strong electric field that causes acceleration may drive a radiation process (see e.g. [RK10]). The bending of field lines also force the particles onto curved trajectories leading to curvature emission(for example [Stu71]). While reasonable in the infrared and shorter wavelength regime[CL02] these approaches do not account for radio emissions since the power output simply turns out to be too small and the timescales involved too large. Lots of efforts have been made to compensate for that by some kind of bunching mechanism, be it electron-positron avalanches at polar caps or the outer gap region (the region before the open field lines cross the light cylinder). When bunched, a mechanism of this kind is radiating coherently and goes as N^2 unless limited by total energy loss considerations. Even though lot of effort was put in these kind of models, they have been considered to fail to explain the radio emission since i) a satisfactory bunching mechanism could not be found ii) bunches would disperse too fast [Mel78a]. This failure gave way to examine elementary coupling mechanisms of plasmas. On one hand elementary plasma waves like Alven or Langmuir waves were considered being driven by a free energy source provided by curvature radiation. This leads to the curvature maser types of mechanisms[LM92]. They depend on a positive distribution gradient in momentum space in the frame of reference for the plasma waves or another free energy source. On the other hand, stream instabilities of various kind were considered, coupled to a free electron maser[Jar05, Sch02]. They naturally exhibit expected behaviour like the short timescale. Most of them were rendered unlikely since the instabilities develop too slow[MG99] or the setup simply seems too artificial and ad hoc. The radio radiation possibly could also be accounted to various processes being coupled or all happening at the same time. However once established, one would get the intensity “for free” out of plasma instability based models given an explanation why the process happens in the strong constrained way outlined in the previous sections and explicitly stated in the following section.

1.6. Constraints to be fulfilled

The two stream instability may drive both a maser or free electron mechanism and is analysed with no concern whatsoever to the radiation process involved. We will only present a chapter estimating two possible radiation process. The main constraints the TSI or a subsequent radio process should reproduce are

1. Coherent radiation output
2. Small emission region
3. Strong bursts on short scale...
4. ...but specific place of occurrence in magnetosphere (for e.g. fingerprint)
5. Polarisation
6. Ubiquitously occurring for broad range of B_0 and P...
7. ...but at rather the same frequency, lengthscales and power output

We refrain from proposing a radio emission mechanism and then trying to analyse its behaviour. Instead, the arguments presented try to establish the inevitability that the two stream instability will happen in pulsar magnetospheres. Then we will derive limits to the instability which naturally will restrict it to parameters that may fit the radiation observed. We will then motivate how a radiation process may be driven by the two stream instability and may "shine a light" onto a radio telescope. We reason that virtually any radiation process based on the TSI may fulfill the characteristics known from observation.

2. Analysis of the two stream instability

> Amongst processes I'm finding
> And schemes that need designing
> With procedures for applying
> And purifying
> *'Procedures' by Amplifier*

2.1. Derivation of the dispersion relation

We are about to calculate the dispersion relation for the two stream instability of a quasi-neutral flow of electrons and positrons. We do this in the cold beam limit, setting the temperature to zero. At background magnetic fields of about 10^{12} Gauss the movement of charged particles is effectively limited to one dimension. Thus a very quick damping of electron/positron movement perpendicular to the field lines by self radiation sets in limiting the movement of both species to trajectories along the field lines. Consequently we will carry out our analysis in 1D. We begin by setting a space constant initial electron positron beam with opposite momenta $\pm p_0$ and densities n_o. We add a small harmonic disturbance $\delta n_0 \exp[i(\omega t \pm kx)]$.

$$f_{\substack{\text{positron}\\ \text{electron}}} = f_{\pm}(x,p,t) = \delta(p \pm p_0)(n_0 + \delta n_0 \exp[i(\omega t \pm kx)]) \tag{2.1}$$

The phase space distribution functions are governed by the Vlasov equation(see also method's sec. B.1.2) stated here. The last term on the left hand side implements the force exerted on the phase space element. In our case it suffices to consider the electromagnetic force generated by the fields of the overall charge distribution. We do not need to implement a Boltzmann term modelling collisions since this term is - as often in astrophysics - negligible for the plasma being thin enough.

$$\partial_t f + v \partial_x f + (\partial_p f) F = 0 \tag{2.2}$$

Since we carry out a linear analysis we can neglect the contributions of currents and thus neglect the magnetic term leaving only electrostatic forces. Inserting our distribution functions (2.1) into the Vlasov equation (2.2) we get the following equations with a yet to be determined electric field E.

$$\delta(p \pm p_0)\delta n_0 \exp[i(\omega t \pm kx)]i[\omega \pm kv] \quad \pm \quad (\partial p f_\pm)Ee = 0 \tag{2.3}$$

The electric field is to be calculated using Gauss's law. We emphasize that the ± signs in the last line of (2.4) just express two ways of writing the same formula whilst in (2.3) they mean two independent equations.

$$\begin{aligned}\nabla E &= 4\pi \sum_\pm (\pm e)\rho_\pm = 4\pi \sum_\pm (\pm e) \int \mathrm{d}p f_\pm \\ E &= 4\pi e \delta n_0 \int \mathrm{d}x \exp[i\omega t](\exp[ikx] - \exp[-ikx]) = \\ &= -i4\pi e\delta n_0 \frac{1}{k}\exp[i\omega t \pm kx](1 + \exp[\mp 2ikx])\end{aligned} \tag{2.4}$$

Let us insert this into (2.3) and divide through the common factor $i\delta n_0 \exp[i(\omega t \pm kv)]$. Now it comes clear why we expressed the electric field in two ways.

$$\delta(p \pm p_0) \mp 4\pi e^2 \frac{\partial_p f}{(\omega \pm kv)k}(1 + \exp[\mp 2ikx]) = 0 \tag{2.5}$$

Let us now integrate over momentum space. The first term leaves us with a 1, the second one needs a bit more attention. Let us first calculate

$$\int \mathrm{d}p \frac{\partial_p f}{\omega \pm kv} \overset{\text{P.I. of } \delta()\text{in f}}{=} -\int \mathrm{d}p f \partial_p \frac{1}{\omega \pm kv} =$$

We can rewrite the partial integral as $\frac{\partial}{\partial p} = \frac{\partial v}{\partial p}\frac{\partial}{\partial v} = \frac{1}{m\gamma^3}\frac{\partial}{\partial v}$ and carry that out

$$= \pm \int \mathrm{d}p f \frac{1}{\gamma^3 m}\frac{1}{(\omega \pm kv)^2}k = \tag{2.6}$$

$$= \pm \frac{1}{\gamma_0^3 m}\frac{1}{(\omega \pm kv_0)^2}k(n_o + o(\delta n_0)) \tag{2.7}$$

Where zero indices of γ_0 and v_0 indicate that these are parameters depending on p_0 and not variables any more. Inserting this back into (2.5) we get the following two equations for positrons and electrons,respectively:

$$1 - \underbrace{\frac{4\pi e^2 n_0}{m\gamma_0^3}}_{\omega^2_{p,\mathrm{rel}}}[1 + \exp[\mp 2ikx]]\frac{1}{(\omega \pm kv_0)^2} = 0 \tag{2.8}$$

where we have omitted the term of $o(\delta n_o)$. We may do so since this term is a quadratic contribution, keeping in mind that we've divided by a factor of δn_0 earlier. Multiplying the equations with $\exp[\pm ikx]$ and adding them we get

$$2\cos(kx) = 2\cos(kx)\omega_{p,\mathrm{rel}}^2\left[\frac{1}{(\omega+kv_o)^2}+\frac{1}{(\omega-kv_o)^2)}\right]$$

Getting rid of the Cosine factor we finally arrive at the dispersion relation for an equally dense counter-streaming electron positron beam:

$$1 = \omega_{p,\mathrm{rel}}^2\left[\frac{1}{(\omega+kv_o)^2}+\frac{1}{(\omega-kv_o)^2}\right], \text{ where } \omega_{p,\mathrm{rel}} = \sqrt{\frac{4\pi e^2 n_0}{m\gamma_0^3}} \tag{2.9}$$

One finds dispersion relations of this type in standard text books, most commonly for a non relativistic beam into a background plasma, for example in [NW94].

2.2. Analysis of dispersion relation

Having derived the dispersion relation (2.9) we now analyse it w.r.t. stability. Pulling $\omega_{p,\mathrm{rel}}$ into the denominator we can define normalized $\overline{\omega}$ and $\overline{k}$ as

$$1 = \frac{1}{(\frac{\omega}{\omega_{p,\mathrm{rel}}}+\frac{kv_o}{\omega_{p,\mathrm{rel}}})^2}+\frac{1}{(\frac{\omega}{\omega_{p,\mathrm{rel}}}-\frac{kv_o}{\omega_{p,\mathrm{rel}}})^2} = \frac{1}{(\overline{\omega}+\overline{k})^2}+\frac{1}{(\overline{\omega}-\overline{k})^2} \tag{2.10}$$

Multiplying with the denominators and expanding leads to a biquadratic equation:

$$0 = \overline{\omega}^4 - \overline{\omega}^2 2(\overline{k}^2+1) + \overline{k}^2(\overline{k}^2-2) \tag{2.11}$$

$$\Rightarrow \overline{\omega}^2 = 1+\overline{k}^2 \pm \sqrt{4\overline{k}^2+1} \tag{2.12}$$

In order to yield complex roots the right hand side of (2.12) has to be smaller than zero. Since we take $\overline{k}$ to be a purely real quantity[1] both the factor under the root and before it are positive. Thus only the solution with the minus sign will adapt a complex branch. The condition

$$1+\overline{k}^2 < \sqrt{4\overline{k}^2+1} \tag{2.13}$$

leads to the requirement that

$$|\overline{k}| < \sqrt{2} \tag{2.14}$$

---

[1] this restricts our solution to the spatial harmonic case with no evanescent wave solutions

Hence the solutions for a positive sign of $\overline{\omega}$ read

$$\begin{aligned}\overline{\omega}_+ &= \sqrt{1+\overline{k}^2+\sqrt{4\overline{k}^2+1}} \\ \overline{\omega}_- &= \begin{cases} \sqrt{1+\overline{k}^2-\sqrt{4\overline{k}^2+1}} & \text{for } |\overline{k}| \geq \sqrt{2} \\ i\sqrt{\sqrt{4\overline{k}^2+1}-(1+\overline{k}^2)} & \text{for } |\overline{k}| < \sqrt{2} \end{cases}\end{aligned} \tag{2.15}$$

A plot of this dispersion relation can be found in figure (2.1). We get the maximum

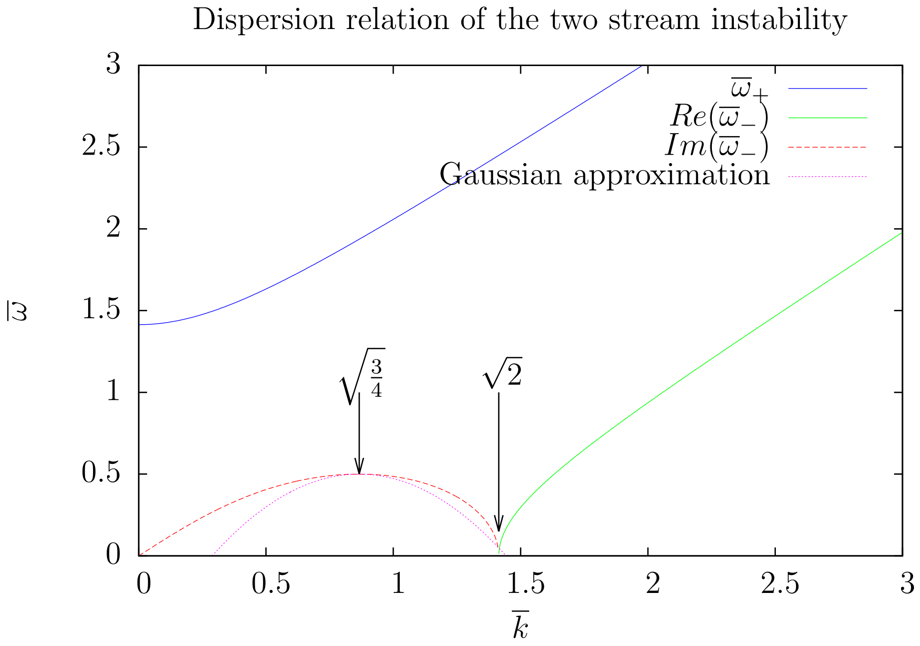

Figure 2.1.: Plot of the dispersion relation of the two stream instability. Plotted in dashed red is the unstable mode of exponential growth.

unstable mode of (2.15) by setting the derivative of the imaginary branch to zero yielding

$$\overline{\omega}_{\max} = \frac{i}{2} \qquad \text{at} \qquad \overline{k}_{\max} = \sqrt{\frac{3}{4}} \tag{2.16}$$

or expressed in absolute quantities

$$\Gamma_{\max} = \frac{\omega_{p,\text{rel}}}{2} \tag{2.17}$$

$$k_{\max} = \sqrt{\frac{3}{4}}\frac{\omega_{p,\text{rel}}}{v_0} = \sqrt{\frac{3\pi e^2 n_0}{m}}\sqrt{\frac{1}{c^2\gamma_0(\gamma_0^2-1)}} \tag{2.18}$$

Later on we want to have some estimate on the timescale and dimensions of the arising wavepackets until nonlinear effects kick in. Since the growth rate of $\frac{\omega_{p,\mathrm{rel}}}{2}$ is quite strong, we expect the two stream instability to form only very short wavepackets of a few plasma wavelengths before entering the nonlinear regime. Being generated out of white noise[2] we can derive an approximate solution with Gaussian envelope and study it's properties. In order to do so we approximate the dominant imaginary part of the dispersion relation by a parabola. Deriving (2.15) w.r.t. $\overline{k}$ twice and evaluating this at $\overline{k}_{\max}$ we gain the value of it's curvature,$-\frac{3}{2}$, and conclude

$$\overline{\omega} \approx -\frac{3}{2}(\overline{k} - \overline{k}_{\max})^2 + \frac{1}{2} \tag{2.19}$$

This approximation is depicted in figure (2.1). Having derived the linear solution to the Vlasov equation(2.2), we can immediately superpose a white noise spectrum initial distribution, $f \pm (k, \pm p, t = 0) = \mathrm{const} \cdot f(p)$ to study the evolution of the instability:

$$\begin{aligned} f_+(x,p,t) &= \delta(p+p_0)\left(n_0 + \delta n_0 \int \mathrm{d}\overline{k} \exp[i(\overline{w}\overline{t} + \overline{k}\overline{x})]\right) \\ &= \delta(p+p_0)\left(n_0 + \delta n_0 \int \mathrm{d}\overline{k} \exp[(-\frac{3}{2}(\overline{k} - \overline{k}_{\max})^2 + \frac{1}{2})\overline{t} + i\overline{k}\overline{x})]\right) \end{aligned} \tag{2.20}$$

Over-lined variables are dimensionless quantities we have to normalize at the end to get the solution with correct units. Getting rid of the δ-function by integrating over p and just looking at the white noise perturbation we yield

$$\begin{aligned} \delta f(x,t) &= \delta n_0 \int \mathrm{d}\overline{k} \exp[\underbrace{(-\frac{3}{2}(\overline{k} - \overline{k}_{\max})^2 + \frac{1}{2})\overline{t}}_{\text{part I}} + \underbrace{i\overline{k}\overline{x}}_{\text{part II}})] \\ &= \delta n_0 \exp[(\frac{1}{2} - \frac{3}{2}\overline{k}^2_{\max})\overline{t}] \int \mathrm{d}\overline{k} \exp[-\frac{3}{2}\overline{t}(\overline{k} - \overline{k}_{\max} + \frac{i\overline{x}}{3\overline{t}})^2] \cdot \\ &\qquad \cdot \exp[\frac{3}{2}\overline{t}(\overline{k}^2_{\max} - \frac{2}{3\overline{t}} i\overline{k}_{\max}\overline{x} - \frac{\overline{x}^2}{9\overline{t}^2}] \\ &= \delta n_0 \exp[\frac{1}{2}\overline{t}] \cdot \exp[-i\overline{k}_{\max}\overline{x}] \sqrt{\frac{2\pi}{3\overline{t}}} \exp[-\frac{\overline{x}^2}{2 \cdot 3\overline{t}}] \end{aligned} \tag{2.21}$$

Reintroducing units and scaling might look cumbersome at first sight. However keeping in mind that part I of (2.21) comes from $\overline{\omega}\overline{t}$, we conclude that $\overline{t} = t\omega_{p,\mathrm{rel}}$ using the definition of $\overline{\omega}$ in (2.10). We analogous conclude from part II that $\overline{x}$ is to be substituted with $\frac{\omega_{p,\mathrm{rel}}}{v_0}x$. Thus we end up with

---

[2] noise equally strong in the whole k-space considered

$$f(x,t) = \delta n_0 \exp[\frac{\omega_{p,\mathrm{rel}} t}{2}] \cdot \exp[-ik_{\max} x]\sqrt{\frac{2\pi}{3t}}\exp[-\frac{x^2}{2 \cdot 3 \frac{v_o^2}{\omega_{p,\mathrm{rel}}} t}] \tag{2.22}$$

This describes an exponentially growing, standing wave with a k-vector of $k_{\max}$ and Gaussian envelope. The width of the package as a function of t is

$$\Delta x(t) = 2\sqrt{3t\frac{v_0^2}{\omega_{p,\mathrm{rel}}}} \tag{2.23}$$

2.3. Structure formation and limits of application

But under which conditions and to what extend are these wavepackets formed before they vanish into nonlinear effects? Clearly, the presented approximations do not hold any longer when the perturbation's density equals the background density. This is the case when

$$\begin{aligned} 1 &\approx \frac{\delta n_o(t_{\max})}{n_0} \\ 1 &= \frac{\delta n_0 \exp[\frac{\omega_{p,\mathrm{rel}}}{2} t_{\max}]}{n_0} \end{aligned}$$

leading to a $t_{\max}$ of

$$t_{\max} = \frac{2}{\omega_{p,\mathrm{rel}}} \ln \frac{n_o}{\delta n_0} \tag{2.24}$$

This amounts to a maximum width of

$$\Delta x_{\max} = \sqrt{18 \ln \frac{n_0}{\delta n_0}} \frac{1}{k_{\max}} \tag{2.25}$$

We conclude that the instability can be observed only for a few plasma cycles. For numerical simulation this fact imposes harsh restrictions. What one would like to simulate is a noisy plasma developing the full instability out of the noise at the calculated wavelength of $\lambda_{\max}$. The easiest way to set up this noise in a PIC simulation would be a thermalized electron positron plasma, where the charge density is generated by setting up pairs of electron and positron quasiparticles with average opposite momenta p_0 and a thermalized spectrum. This method avoids the need to calculate any initial coulomb fields because the charge density is zero everywhere. The fluctuations in the charge density due to the finite number of quasiparticles can be described by a Poisson process. Noise introduced by the quantisation of a flow is also often referred to as *shot noise.* The characteristic scale of shot noise is a fuction of the average number of particles in a given volume. For plasma physics and the simulation a reasonable scale is given by the plasma wavelength, $\lambda_{p,\mathrm{rel}} = \frac{2\pi c}{\omega_{p,\mathrm{rel}}}$. Processes smaller than this wavelength can not be followed collectively by the plasma. We may estimate the number of charges populating an elementary volume of plasma interaction as

$$N_{\#} = n \cdot \lambda_{p,\mathrm{rel}}^3 = c^3 \left(\frac{m\gamma^3 \pi}{e^2} \right)^{\frac{3}{2}} \frac{1}{\sqrt{n}} \tag{2.26}$$

E.g. for a pulsar magnetosphere we have a relativistic astrophysical plasma of $n = 10^6 \frac{1}{cm^3}$ or $10^{10} \frac{1}{cm^3}$ (calculated with low γ-factors). This yields about $10^{16} - 10^{20}$ particles in that volume. The impossibility of dealing computationally with such huge numbers[3] of particles have lead to the introduction of quasiparticles. Because of the simbox usually consisting of about 10^5 elementary cells, we are limited to a few hundred quasiparticles per cell each representing a huge amount of real counterparts (see also sec.B.1.2. This choice has huge implications on the shot noise. As a poisson process, the fluctuation of the number of particles per cell, $N_{\#}$ has a standard deviation of $\sigma_N = \sqrt{N_{\#}}$. Thus in a thermalized plasma we expect the particle number per plasma wavelength volume to fluctuate as $\frac{\sigma_N}{N_{\#}} = \frac{1}{\sqrt{N_{\#}}} = \frac{\delta n_0}{n_0}$. Calculating the time of validity(2.24) for the real plasma we find $t_{\max} \approx \frac{50}{\omega_{p,\mathrm{rel}}}$. Our quasiparticle approach optimistically reaches $t_{\max} \approx \frac{7}{\omega_{p,\mathrm{rel}}}$. Thus for white noise, there is no way to directly measure the wavelength or envelope of the rising two stream instability(2.22). Furthermore we aggravate the problem by grid refinement. With the better resolution comes higher frequencies being enlarged. Starting with lots of sharp delta perturbations in position space with no time to interact, the white noise just starts to grow exponentially, just as theory predicts it to do. Only for grid resolutions near the sampling limit of $\lambda_{p,\mathrm{rel}}$ we expect rather stable wavepackets to form. This on one hand can be accounted to less higher modes poisoning the formation. On the other, noise on the scale of the plasma wavelength already has a big component at $\lambda_{\max}$ and we rather do not start with a delta distribution but with a distribution which is already somewhat broader in spatial dimensions and thus sharper in k-space. Figure 2.2.a shows a simulation of a box of $20m \cdot 20m \cdot 500m$ where the resolution is carefully chosen to be near the plasma frequency. The clearly formed bumps of low and high electron density (separated about 20m) are overlapped by a high frequency at the sampling resolution of 1 meter. Fig. 2.2.b depicts the same simulation at a later time where the interaction became nonlinear. Fig. 2.2.c/d show the same simulation done with a three times better resolution. While c is a snapshot of early development, d depicts the same timestep as a. It is immediately evident from the picture that noise has replaced the clearly visible structure formation observed in a.

---

[3] Computationally feasible numbers are 10^9 - 10^{12} per whole simulation

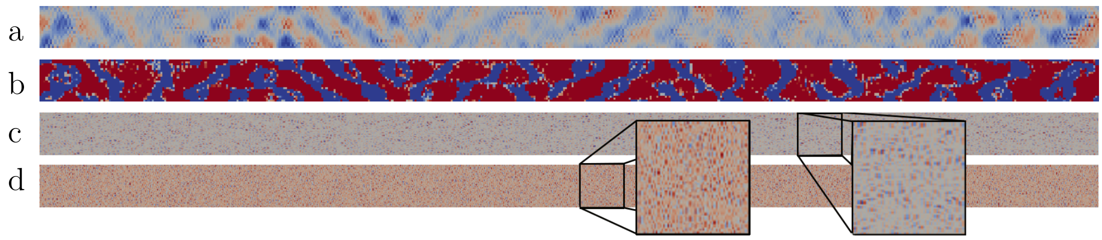

Figure 2.2.: *a*: TSI in a low res simulation allowing for development out of white noise, linear regime. *b*: Nonlinear regime of the same simulation. *c:* early stage of high-res simulation. *d:* simulation at same time as *a* but done with three times the resolution of a and b. For simulation details see table D, a,b: 1c5ab01 c,d: d4643aa.

2.4. Numerical measurement

Having dealt with the peculiarities of a plasma simulation (see sec.B.2), we are able to measure the γ-dependency of the dominant wavelength. This is done varying p_0 in simulation 6d73ddb.. (see sec. D) and analysing every outcome by software. We expect the rise of small wavepackets of different phases. Because the phases do not match, destructive interference occurs and Fourier analysis becomes partly useless for determining the maximal amplified wavelength (see fig.2.3). Only for large mo-

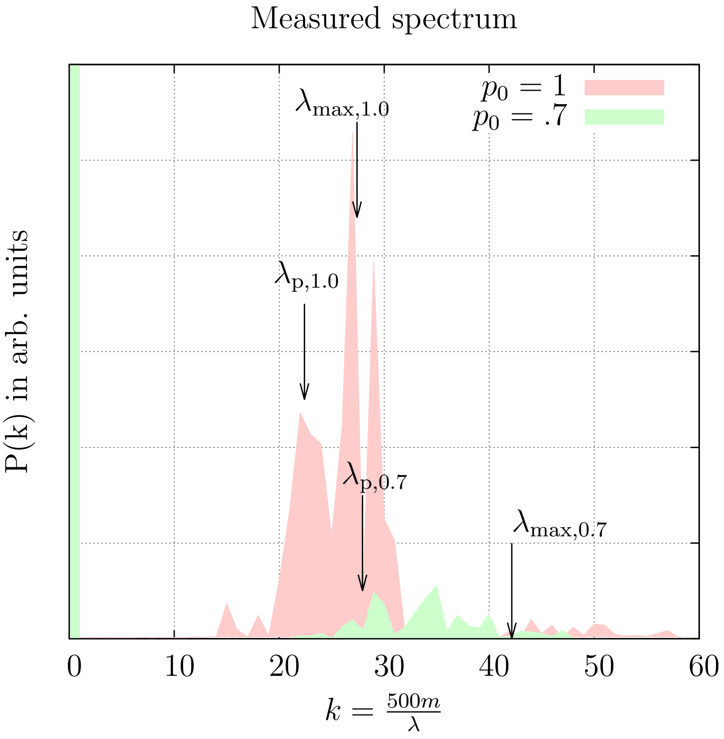

Figure 2.3.: power spectrum of the electron density. For a momentum of $p_0 = 1$ we achieve quite a good resolution in position space and thus have the Fourier transformation reproducing the theoretical expectations for λ_{max}. However, since λ_{max} is quite near the eigenmode of the plasma, we also excite a resonance at the plasma frequency.
The Fourier spectra of the other simulations do not show a peak at the expected frequencies due to destructive interference.

menta we are able to see $\lambda_{\max}$ in the Fourier spectrum since only a few packets fill the whole simbox and destructive interference can not yet average out the signature. However, one can simply measure the desired wavelength taking just one wavepacket in position space. Looking at a typical plot(fig. 2.4) of the electron density, one can verify this fact immediately. A plot as well as a tabular of measured values can be found in figure 2.5.

Measurements and theoretical results are in rather fair agreement taking into consideration lots of error sources. As already argued, the grid resolution has to be low to encounter the instability, leading to a bad sampling at low λ values. One begins to speak of a moderately good sampling if one has more than ten samples per wavelength. This is clearly violated for the higher frequencies, remembering that we simulate on a grid with 2m spatial distance. Secondly, the wavepackets built up have a total size of about six to eight cycles and their borders are typically disturbed by other packets. Thus the error introduced by these imponderables could be considerably larger than the pure measurement error displayed. Nevertheless we can be more confident of the simulation's results when turning to higher wavelengths until at around $p_0 = 1.5$, when the characteristic length scale becomes so large that we again have a too high resolution.

Evaluating (2.23) at $t_{\max}$ yields a package width of about $2.3 \cdot \lambda_{\max}$ which turns out to be a quite good estimate for the observed widths of 2-4 cycles[4]. Looking closely (2.24) gives a $t_{\max}$ of around a cycle until entering the nonlinear regime. This cannot be true for causalities sake since an instability cannot develop faster in space than the speed of light. Indeed, it does not, as simulation shows. There are about three cycles until entering the nonlinear regime. This is as fast as causality allows.

---

[4] we emphasize the difference between the total size of a wavepacket and it's width, which only can be estimated fitting a Gaussian envelope

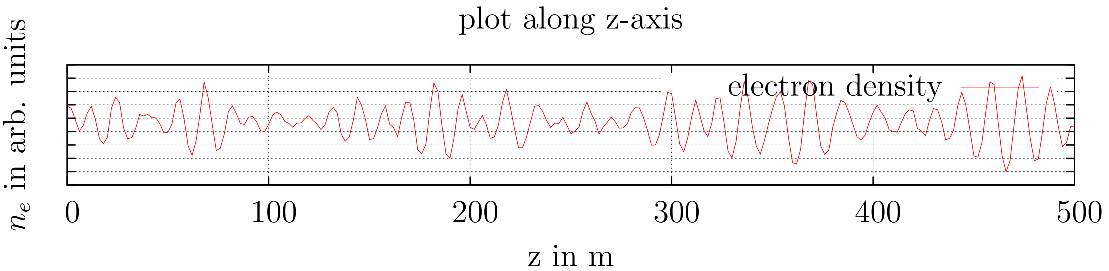

Figure 2.4.: Cut through fully developed TSI-instability. Standing wavepackets of different phases but same wavelength fill the whole space.

p_0	γ_0	λ_p/m	$\lambda_{\max}/m$	$\lambda_{\text{max,measured}}/m$
0.3	1.044	14.16	4.70	7.3 ± 0.8
0.4	1.077	14.83	6.36	9.0 ± 0.8
0.5	1.118	15.69	8.10	10.0 ± 0.8
0.6	1.166	16.71	9.93	11.5 ± 1.3
0.7	1.221	17.90	11.86	12.3 ± 0.8
0.8	1.281	19.23	13.88	15.8 ± 0.8
0.9	1.345	20.71	16.00	$17.2 \pm 1.$
1	1.414	22.32	18.23	19.0 ± 0.8
1.1	1,49	24,05	20,56	22.25 ± 0.6
1.2	1.56	25.91	22.99	23.1 ± 0.6
1.3	1.64	27.87	25.52	24.8 ± 1.0
1.4	1.72	29.95	28.15	30.4 ± 0.6
1.6	1.89	34.39	33.69	30 ± 2

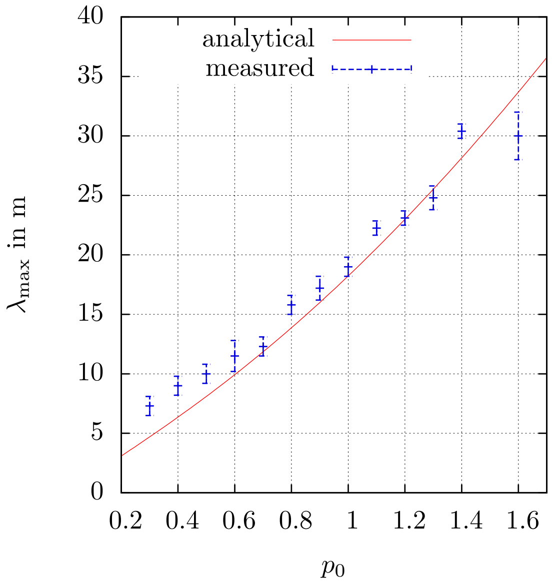

Figure 2.5.: Simulation results as table and plot.

2.5. Concluding remarks on the analysis

As the analysis has shown, the TSI instability is a very strong instability leading to nontrivial structures in an electron-positron beam. It dissipates beam energy into a standing potential structure at a few plasma cycles' time. Calculations as well as high resolution simulations suggest that the instability cannot develop it's characteristic structure out of white noise. However if a suitable substructure in the beams is given, the TSI may form coherent patterns. We've simulated exactly such a substructure by shot noise on scales near the instability's characteristic wavelength.

In general, the typical patterns formed by the TSI are coherent on small scale of a few plasma wavelengths, but phase shifted at larger scales. This has high influence on coherent emission processes. The built up regions of shifted phase tend to interfere destructively if the possible emission process is phase coupled to the regions of the TSI perpendicular to the beam.

Numerically we were able to reproduce the theoretical analysis up to the limits of both physics and simulation. We could have merely worked with a distinct subpattern already containing the characteristic wavelength. This was done before for example by Jaroscheck([Jar05]). Instead we decided for a simple noise pattern yielding the instability's characteristic without seeding it. The code passed this test well enough to proceed to a more advanced setting implementing a strong E_z-field.

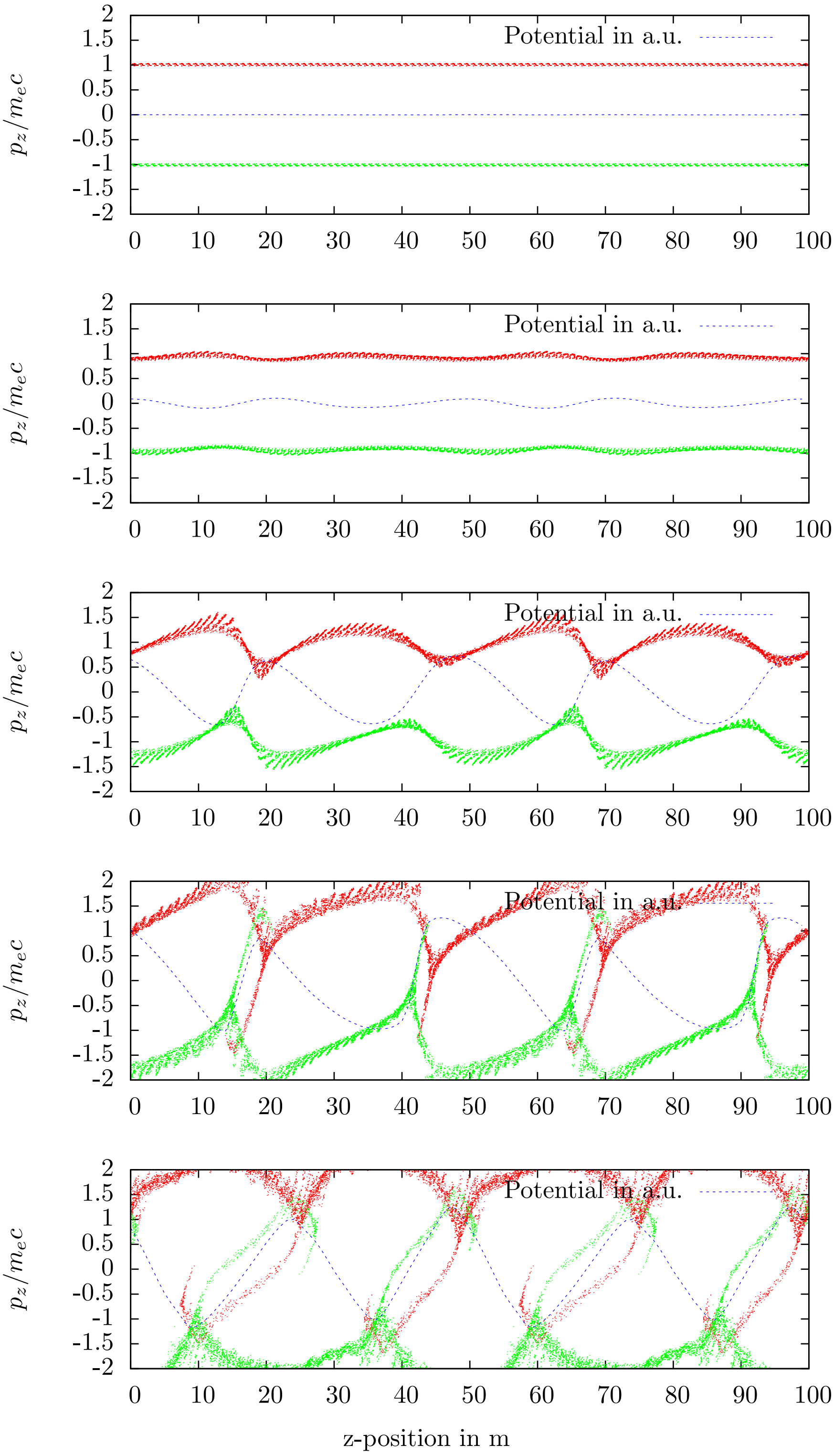

timestep 0:
Simulation is initialized with $p_\pm = \pm 0.8 m_ec$

timestep 100-250:
TSI starts to build up, linear regime

timestep 300:
Instability enters strongly nonlinear regime

timestep 325:
Electrons and positrons begin to mix in phase-space

timestep 350:
Potential is dominated by charge slabs, the TSI is no longer happening

Figure 2.6.: Phasespace plots. Positron quasiparticles are depicted in red, electron quasiparticles are plotted in green.

2.6. The nonlinear regime - an outlook

Analysing the phasespace of a typical TSI instability (see simulation 440eb8b... in sec. D,phasespace plots fig.2.6,some annotations about potential integration in sec. B.3) one immediately notices that when the TSI is showing, the symmetric sinusoidal solutions derived have already developed asymmetries. This can be motivated putting together the pieces of knowledge gained in linear analysis. The TSI is a fast instability of the overall potential and thus a collective effect, but the potential itself is generated by the particles. The particles themselves are slowed down or sped up by the potential gradient, not the absolute value of the potential. Thus if the potential would remain constant, in regions of high potential, the positrons are slow and the electrons are fast. In regions of low potential, electrons are fast and positrons are slow.

But since the potential is changing faster than electrons and positrons are passing it,slow positrons on the height of the potential are lifted without energy loss and flow away from the highest point without being kept there. Positrons right before the potential maximum see a growing potential mountain before them and thus slow down. Thus we expect a pileup of positrons before the maximum of potential energy due to the growth of the potential. This will move the maximum potential further to the left. For the electrons, the situation is vice versa leading to a shift of the minimum to the right. This we can observe happening between plots 2 and 3.

Because of the potential speedily growing higher than the kinetic energy, we expect some positrons and electrons not to have enough energy to pass the potential bumps. They are reflected and enter the attractive flow of the opposite species, accelerated by the steep gradient between the two potential extrema and being attracted by the opposite species' agglomeration. This can be seen in plot 4.

As every species' constituents collect in low-speed areas, we expect an increasing density there, leading to a domination of the potential by that species in this area. In high speed but low density regions, the species does not contribute much to the potential since the low charge density is simply not enough to put a considerable weight in Poisson's equation.

Thus if one species dominates the other, it will carry the potential in it's own direction of movement, since the dispersion relation will become asymmetric. This can be seen in picture 4 to 5. After that the bridge between the electron and positron breaks down. The built up potential starts to oscillate since slabs of electrons and positrons are periodically passing each other.

The TSI clearly provides a standing potential which could cause particles of higher gamma factors than those involved in forming the TSI to radiate coherently. Before turning to the question what kind of radiation could be produced by such a standing potential grid, let us examine where exactly the instability could possibly take place in a pulsar magnetosphere. The presented standing potential is a typical instance of a dynamical equilibrium. Since a charge separation is very sensitive to an electric field, we want to derive some estimate how such a field influences the flux balance vital to form a two stream instability.

3. Damping the TSI

No matter how closely I study it
No matter how I take it apart
No matter how I break it down
It remains consistent.
I wish you were here to see it.
'Indiscipline' by King Crimson

In the following we will discuss the interplay between a paraxial electric field and the two stream instability. On one hand the field flattens arising density bumps by pulling charge carriers apart, on the other hand it pumps energy into the beam, constantly shifting the resonant wavelength. We will discuss both effects and their interplay with the TSI. Then follows a numerical study to verify our findings. We will close the chapter by applying the standard Goldreich-Julian model to our results and estimating the minimal radius at which the TSI may develop in an idealized pulsar magnetosphere.

3.1. Damping by stretching

One of the most basic features of a charged particle is the fact that it is accelerated by electric fields. For an electron in a one dimensional space with electric potential $\Phi(x)$ we may find by using the conservation of energy in the contraction of the 4-momentum, $p_\mu p^\mu$:

$$(E_0 + e\Phi(x))^2 - (p(x)c)^2 = (m_e c^2)^2 \tag{3.1}$$

where $E_0 > m_e c^2$we solve this for p and get

$$p(x) = \frac{1}{c}\sqrt{(E_o + e\Phi(x))^2 - (m_e c^2)^2} \tag{3.2}$$

From here on, let us normalize the momenta with $m_e c$ where not otherwise stated. We now consider two equally charged particles streaming through this potential a small distance L apart from each other, small but big enough to neglect their repulsive force. Since they are both moving in the same potential, equation (3.2) tells us that they will do so at different momenta. We calculate their relative speed given their relative momentum $p_1 - p_2 = p_\Delta$. For convenience we define $p_1 =: p + \Delta$ and $p_2 =: p - \Delta$ such that $p_\Delta = 2\Delta$. We assume $\Delta \ll p$. Since $p = \gamma\beta = \frac{\beta}{\sqrt{1-\beta^2}}$, $\beta(p) = \sqrt{\frac{p^2}{1+p^2}}$ and we can calculate the relative speed as seen from the rest frame:

$$\begin{aligned}
\Delta\beta = \beta_1 - \beta_2 &= \sqrt{\frac{(p+\Delta)^2}{1+(p+\Delta)^2}} - \sqrt{\frac{(p-\Delta)^2}{1+(p-\Delta)^2}} = \\
&= \frac{\sqrt{(p+\Delta)^2(1+(p-\Delta)^2)} - \sqrt{(p-\Delta)^2(1+(p+\Delta)^2)}}{\sqrt{(1+\Delta^2+p^2)^2 - 4p^2\Delta^2}} = \\
&= \frac{(p^2-\Delta^2)(\sqrt{1+\frac{1}{(p-\Delta)^2}} - \sqrt{1+\frac{1}{(p+\Delta)^2}})}{\sqrt{(1+\Delta^2+p^2)^2 - 4p^2\Delta^2}}
\end{aligned}$$

Since Δ w.r.t. p is small, we can expand the roots of the numerator as $\sqrt{1+\frac{1}{(p\mp\Delta)^2}} \approx \sqrt{1+\frac{1}{p^2}} + \frac{1}{\sqrt{1+p^2}p^2}(\pm\Delta)$ yielding

$$\begin{aligned}
&= \frac{(p^2-\Delta^2)2\Delta}{\sqrt{1+p^2}p^2\sqrt{(1+\Delta^2+p^2)^2 - 4p^2\Delta^2}} \approx \\
&\approx \frac{2\Delta}{(1+p^2)^{3/2}} = \frac{p_\Delta}{\gamma^3}
\end{aligned} \tag{3.3}$$

Consequently, the distance between the two particles increases like

$$\Delta L = \Delta t \Delta\beta c = \Delta t c \frac{p_\Delta}{\gamma^3}$$

where we can approximate $p_\Delta = \frac{\mathrm{d}p}{\mathrm{d}x} L$

$$= \Delta t \Delta\beta c = \Delta t (\frac{\partial p}{\partial dx}\frac{c}{\gamma^3}) L \tag{3.4}$$

bringing L and Δt to the left and taking the infinitesimal limit we get

$$\frac{\frac{\partial L}{\partial t}}{L} = \frac{\partial p}{\partial x}\frac{c}{\gamma^3} =: \Gamma_{acc} \tag{3.5}$$

Thus we expect the length scale of the distance of the two electrons to increase exponentially with a growth rate determined by eq. (3.5). Inserting (3.2) into Γ_{acc} yields:

$$\Gamma_{acc} = \underbrace{\frac{1}{\gamma^3}\frac{E_0 + e\Phi}{\sqrt{(E_0 + e\Phi(x))^2 - (m_e c^2)^2}}}_{\text{inertial suppression}} \underbrace{\frac{e}{m_e c}\frac{\partial\Phi}{\partial x}}_{\text{field driven part}} \tag{3.6}$$

We immediately grasp that Γ_{acc} factors into a part suppressed by the relativistic movement of the electrons and another part which solely depends on the gradient of the potential, the electric field.
If the potential is not dominated by our charge distribution but mainly by some external field, this result carries over to fluctuations in a charge distribution. Especially for a periodic disturbance in an otherwise neutral current, the assumptions presented are still valid. Contributions of the disturbance to the fields may be neglected since the oscillating density averages out through Gauss's law. Since charge is conserved, disturbances in the charge density are not just shifted to higher wavelengths, also their amplitude becomes smaller.

3.2. Comparison of damping and amplification

Before we examine the pumping of energy into the plasma, let us focus on the interplay between stretching by damping and clumping by the instability. Since the two processes are on first order of the same kind, one naively may compare the two rates of the TSI and the damping. Later on we will see that simple comparison of the rates is not sufficient to understand the dominance of a certain process. Bringing the rates into an appropriate form one gets:

$$\begin{aligned}\Gamma_{acc} &\overset{(3.6)}{=} \frac{1}{\gamma^2\sqrt{\gamma^2-1}}\frac{e}{m_e c}\frac{\partial\Phi}{\partial z}\\ \Gamma_{tsi} &\overset{(2.18)}{=} \frac{1}{\gamma^{3/2}}\frac{\omega_p}{2}\end{aligned} \tag{3.7}$$

For large values of γ the damping diminishes as γ^{-3} while the TSI falls off as $\gamma^{-\frac{3}{2}}$. Thus, given an paraxial electric field, we first of all expect the TSI to be the dominant process above a certain $\gamma_{\max}$ dependent on the non relativistic plasma frequency and the electric field. At beam energies below that $\gamma_{\max}$ the TSI should be suppressed. Above these energies we expect the TSI to limit further acceleration of the beam by building up a strong potential field and slowing down the constituents of the beam if no other constraints have to be considered[1]. For $\frac{\Gamma_{acc}}{\Gamma_{TSI}} = 1$ we derive

$$\sqrt{\gamma_{\max}(\gamma_{\max}^2-1)} := \frac{e}{m_e c}\frac{\partial\Phi}{\partial z}\frac{2}{\omega_p} \tag{3.8}$$

---

[1] Indeed energy gain is such a constraint which we will examine in the next section

and can give the following two approximations for convenience:

$$\begin{aligned}
\gamma_{\max} &= \left(\frac{e}{m_e c}\frac{\partial\Phi}{\partial z}\frac{2}{\omega_p}\right)^{2/3} && \text{for } \gamma_{\max} \gg 1 \\
\gamma_{\max} &= 1 + \frac{e}{m_e c}\frac{\partial\Phi}{\partial z}\frac{\sqrt{2}}{\omega_p} && \text{for } \gamma_{\max} \approx 1
\end{aligned} \tag{3.9}$$

The l.h.s of (3.8) as well as $\gamma_{\max}$ are frequently arising terms in the following analysis and may serve as a translator between field energy and various other variables.

3.3. Detuning by energy gain

Up to now we've neglected the primary effect of an electric field, namely raising beam energy. For a current that is not strong enough to deplete the electric field, we may find the rise of γ as

$$\frac{\mathrm{d}p}{\mathrm{d}t} = m_e c \frac{\mathrm{d}\sqrt{\gamma^2 - 1}}{\mathrm{d}t} = \frac{\partial\Phi}{\partial z} e$$

$$\sqrt{\gamma(t)^2 - 1} - \sqrt{\gamma_0^2 - 1} = \frac{\frac{\partial\Phi}{\partial z} e}{m_e c} t \tag{3.10}$$

$$\gamma(t) = \sqrt{1 + \left(\frac{\frac{\partial\Phi}{\partial z} e}{m_e c} t + \sqrt{\gamma_0^2 - 1}\right)} \tag{3.11}$$

Since the TSI consists of a standing density wave solution, it is vital that the resonant wavelength does not change much over the development timescale. Consequently, the relative shift in γ due to the electric field pumping energy into the system should stay smaller than one during the typical timescale $T_{tsi} = \frac{2}{\omega_{p,\mathrm{rel}}}$. For our analysis is convenient to express the electric field strength in terms of $\gamma_{\max}$ as defined in (3.8). The right hand side of (3.10) then becomes

$$\frac{\frac{\partial\Phi}{\partial z} e}{m_e c} T_{tsi} = \sqrt{\gamma_{\max}(\gamma_{\max}^2 - 1)}\gamma_0^{3/2}$$

Now we can easily evaluate the relative change of γ using (3.11).

$$\frac{\gamma(t_{tsi}) - \gamma_0}{\gamma_0} = \sqrt{\frac{1}{\gamma_0^2} + \left(\sqrt{\gamma_{\max}(\gamma_{\max}^2 - 1)}\sqrt{\gamma_0} + \sqrt{1 - \frac{1}{\gamma_0^2}}\right)^2} - 1 \tag{3.12}$$

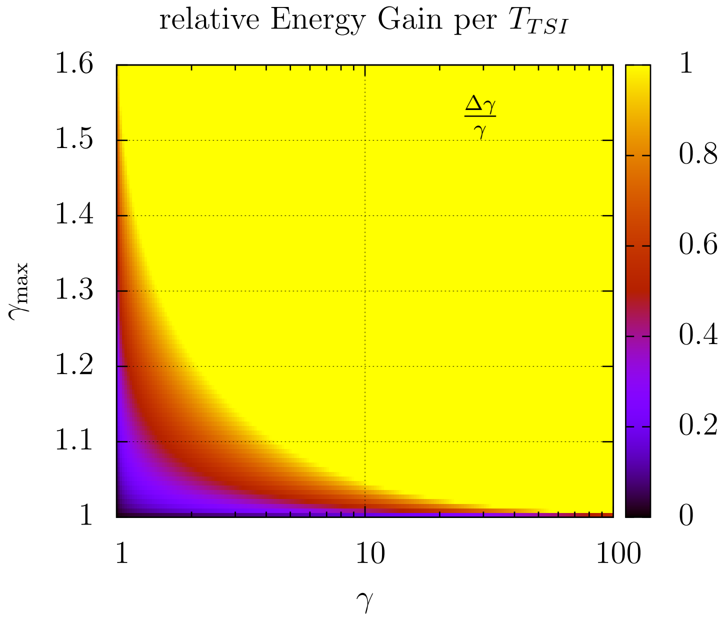

Figure 3.1.: The electric field pumping energy into the beam sets quite low limits on the TSI instability. The TSI instability can only grow efficiently where the relative energy gain is considerably lower than one.

The condition that (3.12) should be small compared to one leads to the following inequality:

$$\sqrt{\gamma_{\max}(\gamma_{\max}^2 - 1)} < \frac{\sqrt{4 - \frac{1}{\gamma^2}} - \sqrt{1 - \frac{1}{\gamma^2}}}{\sqrt{\gamma}} \tag{3.13}$$

Looking at the plot of the relative energy gain in fig. 3.1 one can see that this condition leads to low $\gamma_{\max}$ factors. Nevertheless these factors still amount to relatively high fields, a rule of thumb for a typical plasma density would give the electric field as $E = \sqrt{\gamma_{\max}(\gamma_{\max}^2 - 1)} \cdot 10^5 \frac{V}{m}$.

3.4. Discussion and numerical verification of the criteria

Putting damping by stretching and too high energy gain together we get the exclusion area for the TSI. As one can see in the plot (fig. 3.2) a high electric field is an effective way to damp the instability. The ascending slope in the left part shows up due to the damping by acceleration. Partially it reflects the definition of $\gamma_{\max}$, namely that the strength of damping and instability should be equal. Here of course one is also able to see how steep the balance of powers arises. The right side of the

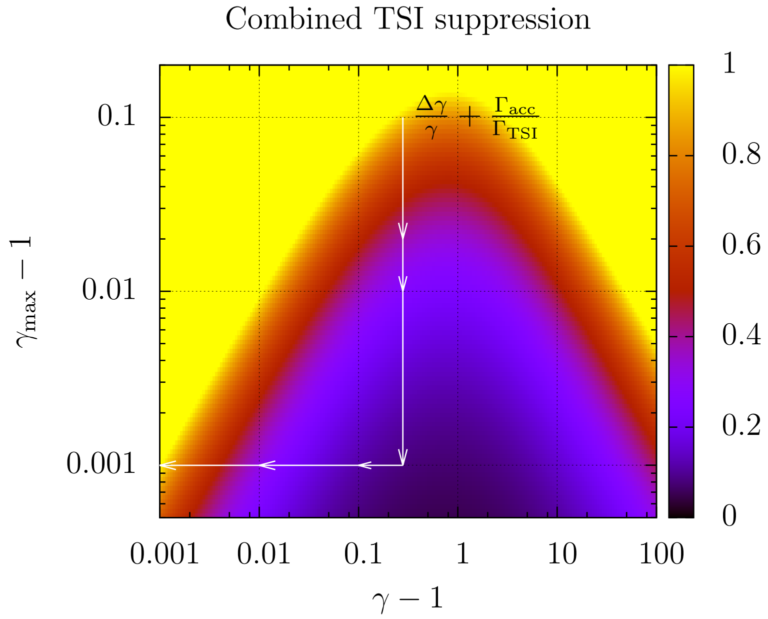

Figure 3.2.: This plot shows the combination of both the energy gain criterion and the damping by acceleration. Since γ_{max} is just defined to be the border between the domination of the damping by acceleration the upper diagonal part of the graph does not allow for the TSI to develop. The white arrows show the parameters' path of the simulations conducted to experimentally verify the borders of validity.

graph is dominated by the energy gain condition. Since both formulae are more or less approximative, we conclude that there is an area around $\gamma = 2$ that allows the two stream instability for the highest values of the electric field. We tested (see simulations 2f0c4f1..,11181c9.. in table D,setup description in section B.2.3)the derived behaviour for the white path within the figure. We expect the TSI to show up at the lower values of the vertical path. Then, proceeding to the left, we expect the TSI to saturate at some wavelength where enough energy has been pumped into the beam to reach γ_{max} from the starting value of γ. Whereas the descent to low γ_{max} yielded no growth of the instability, slices through the xy-plane of the horizontal path exhibit the desired behaviour, see figure 3.3. The following table shows a summary of the observations gained.

γ	γ_{max}	observation
1.28	1.1	no TSI
1.28	1.02	no TSI
1.28	1.01	no TSI but constant noise
1.28	1.001	TSI, even though not strong
1.1	1.001	strong TSI with good transversal phase synchronisation
1.01	1.001	TSI at lower wavelength
1.001	1.001	TSI converges at lower wavelength
1.0001	1.001	nearly the same as the simulation before

We conclude that we find fair agreement between theory and simulations. The be-

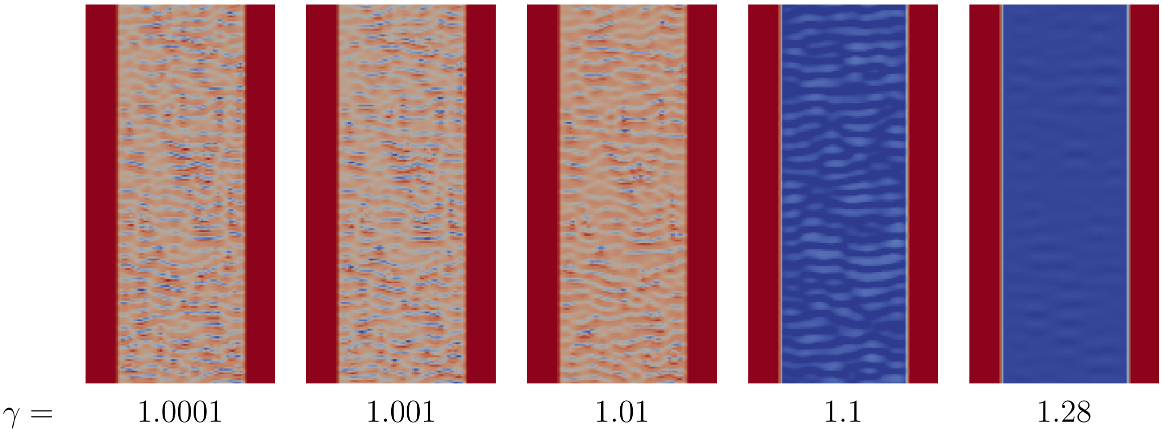

Figure 3.3.: xz-plane slices through the electron density of simulations with $\gamma_{\text{max}} = 1.001$. the similar positions of the waves is due to same random initialization. (simulations: 2f0c4f1..,11181c9.., see section D)

ginning of suppression of the TSI at $\gamma_{\text{max}} = 1.001, \gamma = 1.28$ might at first sight come as a surprise since the relative energy gain at that point amounts only to about 10%. However, if one calculates the shift in resonant wavelength, one yields a shift of about 40% during the typical TSI's period. It becomes clear that the TSI is still quite suppressed because of the potential differences in configuration space get out of resonance quickly.

3.5. Application to pulsar model

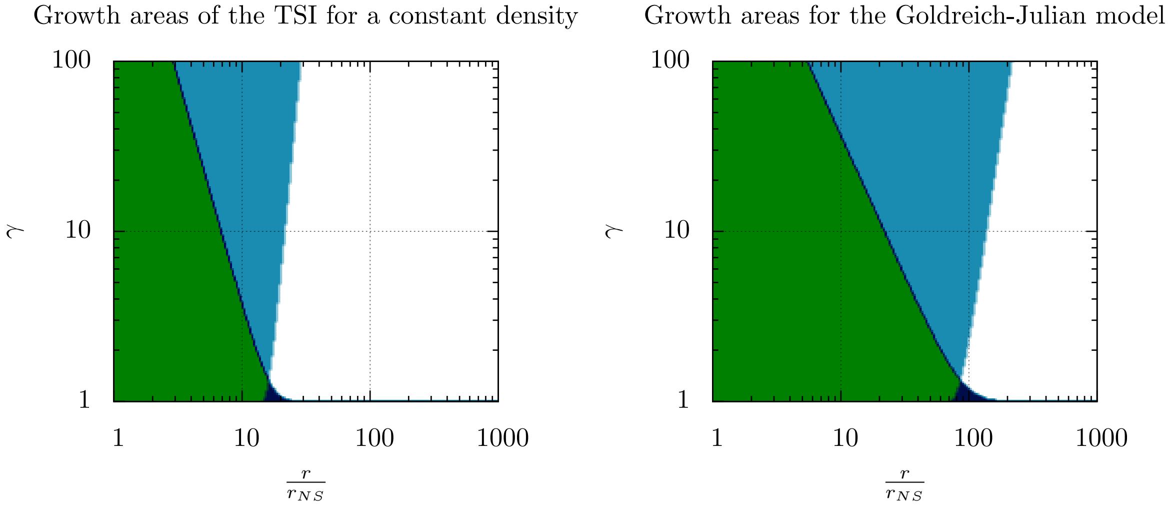

Figure 3.4.: This plot shows the region where the TSI can grow in white. The light blue extension is where only the strength criterion(3.8) is met, whereas the dark blue area marks the fulfilment of only the energy gain criterion (3.13). The green area misses both criteria

Let us briefly recall the features of the Goldreich-Julian model introduced in the introduction(sec.1.3). While it is still unknown to what extent the model is valid it is nevertheless a solid point to start for several reasons. Leaving aside the open field lines it should provide an acceptable approximation of the charge difference on closed field lines. Closed field lines are expected to dominate the pulsar's inner magnetosphere. Since they trap charges effectively the assumption of a static magnetosphere of Goldreich and Julian is a way to derive a reasonable net charge of the field configuration. Thus we expect the falloff of the field to be somewhere near the GJ approach. Reminding ourselves about the possible space charge effects and suchlike phenomena, we can take the Goldreich-Julian density to be a hint. That is why we decided for two plots (fig 3.4) of the TSI-exclusion regions found in (3.8) & (3.13). Both graphics are calculated for a pulsar of radius $10km$, a period of $0.5s$ and a B_0 of $10^{12}G$. The first plot shows the exclusion region for a GJ-like parallel electric field while leaving the charge density constant to the value it has at r_{NS}. The second one is calculated with a varying density profile after Goldreich-Julian.

For the sake of completeness we state here the relevant parameters of evaluation:

$$E(r) = \left(\frac{r_{NS}}{r}\right)^4 1.26 \cdot 10^{12} \frac{V}{m}$$
$$n_{GJ}(r) = \left(\frac{r_{NS}}{r}\right)^3 1.39 \cdot 10^{11} \frac{1}{cm^3} \tag{3.14}$$

Since the non relativistic plasma frequency enters the formulae at the same place like the electric field, one sees immediately that the form of the density only remaps the radius axis. Thus, for a higher multiplicity ζ the minimal radius of the TSI is again decreasing. it is easy to see that r_{min} scales with multiplicity as

$$r_{min} \propto \zeta^{1/(\beta-2\alpha)} \tag{3.15}$$

where α is the exponent of the electric field and β the exponent of the density in (3.14). For the GJ model, $\alpha = 4, \beta = 3$ thus the minimal radius scales as $r_{min} \propto \sqrt[5]{\frac{1}{\zeta}}$ with multiplicity. We conclude that multiplicity has a low influence on the considerations taken, but shifts the minimal TSI radius inwards for higher values.
To estimate the TSI's minimal radii for a whole population of pulsars, we estimate a maximum field strength at which the TSI is still strong enough to develop. This is done by fulfilling (3.13) with a $\gamma \approx 1$ on the r.h.s. . This leads to $\gamma_{\max} \approx 1.67$ which is way too high in sense of observed TSI dependence. However, shielding some part of the field the core of the current might be subject to a fairly lower electric field and undergo TSI. We may now insert $\gamma_{\max}$ as well as the field and density dependence of the GJ-model(see sec. 1.3 for calculations into (3.8) and solve this for r_{min}/r_{NS} to yield:

$$\frac{r_{min}}{r_{NS}} \approx \left(\frac{2e}{3mc^3}\frac{B_o \Omega r_{NS}^2}{\zeta}\right)^{\frac{1}{5}} \tag{3.16}$$

This amounts to a maximum resonant wavelength of

$$\lambda_{\max} = \underbrace{\sqrt{\frac{2\pi m}{3e^2 n}} c}_{\lambda_{\text{scale}}} \sqrt{\gamma(\gamma^2-1)} \tag{3.17}$$

$$\lambda_{\text{scale}} = \sqrt{\frac{8\pi^2 c}{3e}} \left(\frac{2}{3mc^3}\gamma^3 r_{NS}^2\right)^{\frac{3}{10}} c \cdot$$
$$\cdot \left(\Omega B_o\right)^{-\frac{1}{5}} \zeta^{-\frac{3}{10}} \tag{3.18}$$

where the γ expression λ_{scale} typically takes values of 10^{-2} to 10^{-1}. Plotting both parameters and overlaying a pulsar population as seen in fig. 3.5 shows: We expect a very narrow range of about one magnitude of minimal radii even though the input parameters, period and magnetic field, both vary over a few magnitudes. Also the scaling wavelength exhibits a scaling of roughly a magnitude over the whole popula-

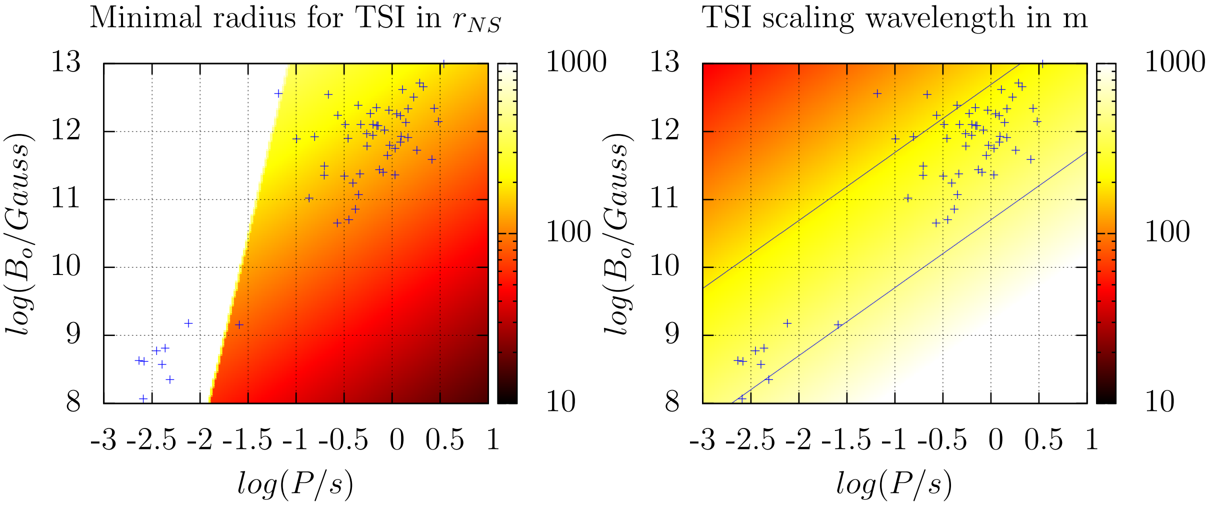

Figure 3.5.: Estimation of minimal TSI radius and characteristic scale at that point. The white area at the upper left is the light cylinder limit, see text.The contour lines of the second plot are drawn at 100m and 500m. The pulsar sample is taken from the ATNF database[Fac12].

tion. Considering the absolute value of the scaling wavelength and reminding us of the two orders of magnitude we loose to the γ-dependent term, we arrive at scales in the desired MHz range one observes the radio emissions with a radio telescope. Even though these calculations should be taken with care regarding the absolute values obtained, they show promising scaling and astonishing agreement with the observed radio output. However, the model presented does not explain the short period pulsars' behaviour, since the minimal radius for the TSI to happen exceeds the light cylinder radius. Many radiation processes suffer from not being able to explain this limit of short light cylinder. In this case we account this to a too conservative estimation of $\gamma_{\max}$ since in reality the shielding of the parallel E-field by the current could be much bigger than silently assumed here by ad hoc arguments. Further studies should examine this point rigorously.
We will in the following motivate why the TSI might drive a radiating process and give at least an estimation of the brightness achieved.

4. Two processes of radio radiation

Oh, my something in my eye eye
Something in the sky sky
Waiting there for me
'Let there be more light'
by Pink Floyd

Even though we've shown a lot up to now, there would nothing to be seen with a radio telescope. Up to now we have motivated the existence of a mechanism which itself (in the linear regime) just builds up potential energy, and does not radiate. Let us now examine whether some available background density of high γ or its constituents radiate and estimate the power output of these two processes.

4.1. Radiation by high-gamma background

As we've concluded in chapter 3, the two stream instability in an electric field can only happen at fairly low γ-factors smaller than about 1.1. This makes it quite plausible that there will be some population of higher γ factors. This density does not drive a TSI because of the aforementioned arguments; because of the $\gamma^{-3/2}$ dependency of the growth rate, the detuning of resonance by gain of energy renders the TSI mechanism useless. Nevertheless it may radiate coherently while striving over the potential ripples of the low-γ TSI building up. It is common sense in electrodynamics that one may estimate coherent power output by calculating a single contribution and concluding that

$$\langle P_{\mathrm{coh}} \rangle = \langle P_{\mathrm{single}} \rangle \cdot N^2 \tag{4.1}$$

since all electric fields of single particles may be added neglecting interactions between the particles. Thus the electric field is proportional to N, leading to a N^2 dependence of power output. Both factors N^2 and $< P_{\mathrm{single}} >$ can be estimated using the results of the preceding sections.

Let us start with the TSI's geometry to estimate the number of coherently radiating particles.

$$N = n_{\mathrm{rad}} \cdot V_{\mathrm{tsi}} \tag{4.2}$$

where the volume of the emission region, V_{tsi} is estimated to be about the size of a cylinder of length $2\Delta x_{\mathrm{max}}$ and radius $c \cdot t_{\mathrm{max}}$. The propagation with light speed can be assumed since propagation transversal to the beam is supplied by continuity of fields. The given dimensions on one hand slightly overestimate the geometry since the instability developed out of a located density bump cannot go faster than light (which would be the case on the diagonal), on the other hand it underestimates the size of the region since a damped instability may develop more slowly leading to a greater region of coherence, as shown in the simulations. Inserting (2.24) and (2.25) we find

$$\begin{aligned} N &= n_{\mathrm{rad}}\pi(ct_{\mathrm{max}})^2 2\Delta x_{\mathrm{max}} = \\ &= n_{\mathrm{rad}}\pi(\frac{2}{\omega_{p,\mathrm{rel}}})^3(\ln\frac{n_o}{\delta n_o})^{5/2}2\sqrt{6}c^2 v_o = \\ &= n_{\mathrm{rad}}\pi(\frac{2}{\omega_{p,\mathrm{rel}}})^3(\ln\frac{n_o}{\delta n_o})^{5/2}2\sqrt{6}c^3\sqrt{\frac{\gamma^2-1}{\gamma}} \end{aligned} \tag{4.3}$$

where the γ factor, $n_o, \delta n_o$ and plasma frequency is that of the TSI population, not the radiating one.

Estimating the power output of a single particle takes a bit of work. The generalization of Larmor's formula for the power of radiation of an accelerated particle along the field lines can be found e.g. in [Mel78b], eq. (20). For a relativistic particle one may take the average over space, not time, since the particle spends nearly the same time in every potential region. Notice that in this case, the expression is independent of the γ-factor of the radiating particle distribution. We've settled that matter by rederiving the formula from the relativistic generalization of Larmor's formula in the appendix A.2.

$$\langle P_{\mathrm{single}}\rangle = \frac{1}{T}\int_0^T \mathrm{d}t \frac{2e^2}{3m^2c^3}\left|\frac{\mathrm{d}\Phi}{\mathrm{d}x}|_{x=x(t)}\right|^2 = \frac{2e^2}{3m^2c^3}\langle\left(\frac{\mathrm{d}\Phi}{\mathrm{d}x}\right)^2\rangle \tag{4.4}$$

The potential concerned consists of different parts we add independently, namely the particle's initial energy, the pulsar's potential and the disturbance introduced by the TSI generated by the non radiating population.

$$\Phi = E_o + \Phi_{NS}(r) + \Phi_{TSI}(r) \tag{4.5}$$

E_o vanishes when deriving w.r.t. the spatial coordinate and Φ_{NS}'s characteristic length is fairly longer than the volume we are facing. Thus we only take our term, Φ_{TSI} into consideration, renaming the spatial coordinate to x. By doing so we omit cross terms and focus on radiation we expect to be around λ_{max}. Idealizing the situation, we calculate the electric field of a sinusoidal potential disturbance depleting completely our initial density n_o to a density of zero. Once again integrating Poisson's law in one dimension leads to

$$\begin{aligned}\Phi_{TSI}(x) &= -2\pi n_o e \ \mathrm{d}z(\cos(k_{\max}x) - \cos(k_{\max}x - \pi)) = \\ &= -4\pi n_o e \ \mathrm{d}z \cos(k_{\max}x) \\ &= \frac{4\pi n_0 e}{k_{\max}^2}\cos(k_{\max}x) \end{aligned} \tag{4.6}$$

Thus deriving w.r.t. x leads to a force we may insert into 4.4 and conclude

$$\begin{aligned}\langle P_{\text{single}}\rangle &= \frac{2e^4}{3m^2c^3}\left(\frac{4\pi n_o}{k_{\max}}\right)^2 \langle \sin^2(k_{\max}x)\rangle = \\ &= \frac{e^4}{3m^2c^3}\left(\frac{4\pi n_o}{k_{\max}}\right)^2 \end{aligned} \tag{4.7}$$

Inserting (4.7) and (4.3) into (4.1) and simplifying yields:

$$\begin{aligned}\langle P_{\text{coh}}\rangle &= \frac{e^4}{3m^2c^3}\left(\frac{4\pi n_o}{k_{\max}}\right)^2 \cdot \left(n_{\text{rad}}\pi(\frac{2}{\omega_{p,\text{rel}}})^3(\ln\frac{n_o}{\delta n_o})^{5/2}2\sqrt{6}c^3\sqrt{\frac{\gamma^2-1}{\gamma}}\right)^2 = \ldots = \\ &= \frac{128m^2c^5}{3e^4}\left(\frac{n_{\text{rad}}}{n_o}\right)^2(\ln\frac{n_0}{\delta n_o})^5(\gamma^4(\gamma^2-1))^2 = \qquad (4.8) \\ &= \left(1.62\cdot 10^{37}\frac{Erg}{s}\right)\left(\frac{n_{\text{rad}}}{n_o}\right)^2(\ln\frac{n_0}{\delta n_o})^5(\gamma^4(\gamma^2-1))^2 \qquad (4.9)\end{aligned}$$

The last two factors account to a loss of about three to four orders of magnitude. We know that the TSI breaks down relatively fast and might take long times to recover such that the pulsar does only radiate a certain fraction of time. This way we could lose another two orders of magnitude or more concerning total radio output of a pulsar as well as by opacity of the magnetosphere and effectiveness of the mechanism as a whole. Multiplying these losses we arrive at plausible total radio powers of perhaps $10^{28}Erg/s$ to $10^{32}Erg/s$.

4.2. Self-radiation in nonlinear phase

We've see in simulations that the electrons and positrons of the TSI naturally bunch when entering the nonlinear phase decoupling from the mechanism driving the TSI. In this phase, slabs of electrons and positrons just cross each other collisionless. This causes autopolarisation. Unlike the continuous polarisation idealized from a homogeneous plasma the same happens here but in discrete steps. The force assigned to the displacement of charge carriers does not follow a linear dependency but a step function since every time the slabs cross, we encounter the whole surface charge density while in between, the gradient of the field remains unchanged. Reconsidering

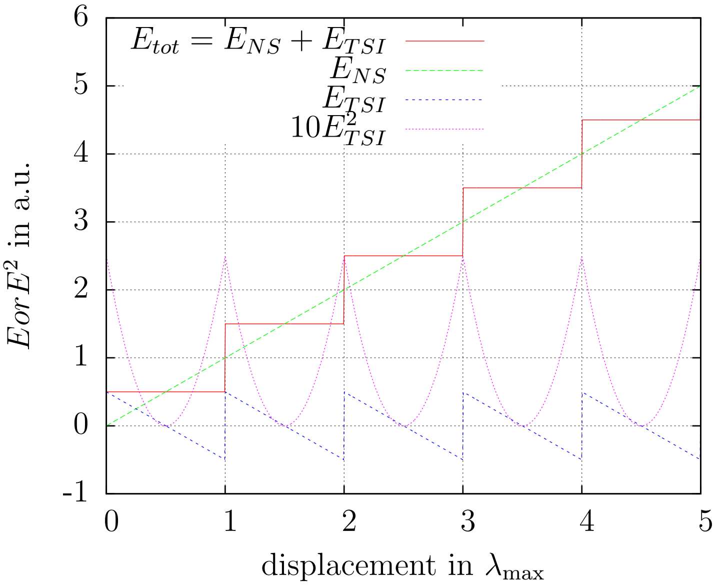

Figure 4.1.: The array of slabs crossing each other generates a step-like E-field on it's constituents

Larmor's formula(4.4) we may split the potential gradient as the sum of a high frequency part and a low frequency part:

$$E_{tot} = E_{NS} + E_{TSI} \tag{4.10}$$

While we expect the low frequency part to couple with the overall electric field in the magnetosphere, the high frequency part again is the cause of radio radiation. Fortunately we may again split the averaging in Larmor's formula in two parts and omit the long-range contribution. This is justified by yielding a cross term in the averaging procedure which vanishes (since it is an integral over a piecewise point symmetric sawtooth times a quasi-constant overall electric field). Again, we calculate one such step by integrating over one charge slab and conclude that $\Delta E = 4\pi n_o e \frac{2\pi}{k_{\mathrm{max}}}$. As can be seen in figure 4.2, we now need to average over the square of an electric field which drops linearly from $+\frac{1}{2}\Delta E$ to $-\frac{1}{2}\Delta E$. The average should happen over time, which would in principle force us to reconsider the whole electric field and derive equations of motion. Since the squared E_{TSI} is piecewise symmetric a slight preference of the last part to the first is negligible for a crude estimation. Hence we leave this peculiarity aside and conclude that:

$$\langle E^2_{TSI} \rangle = \frac{1}{1-(-1)} \int_{-1}^{1} \mathrm{d}x (\frac{1}{2}\Delta E(-x))^2 = \frac{\Delta E^2}{12} = \frac{16\pi^4 n_o^2 e^2}{3k^2_{\mathrm{max}}} \tag{4.11}$$

$$\langle P_{\mathrm{single}} \rangle = \frac{32 e^4 \pi^4 n_o^2}{9 m^2 c^3 k^2_{\mathrm{max}}} \tag{4.12}$$

Inserting this together with 4.3 (n_{rad} now equals n_o) into 4.1 we arrive at the maximum expected total energy output:

$$\langle P_{\mathrm{coh,II}} \rangle = \frac{256\pi^2 m^2 c^5}{9e^4} (\ln \frac{n_0}{\delta n_o})^5 (\gamma^4(\gamma^2-1))^2 = \tag{4.13}$$

$$= \left(1.1 \cdot 10^{38} \frac{Erg}{s}\right) (\ln \frac{n_0}{\delta n_o})^5 (\gamma^4(\gamma^2-1))^2 \tag{4.14}$$

4.3. Coupling of different processes and real radiative output

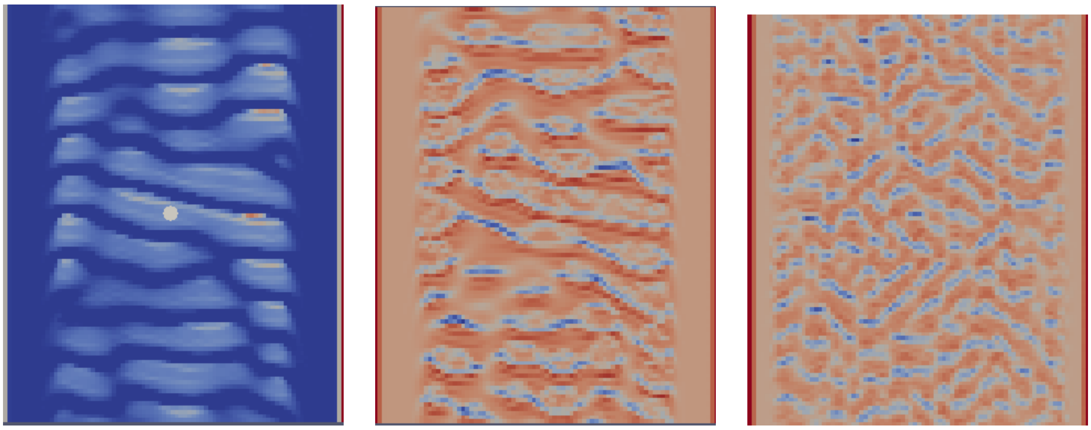

$n_{rad} = 0\% n_o$ $n_{rad} = 10\% n_o$ $n_{rad} = 100\% n_o$

Figure 4.2.: Different radiating background densities lead to different types of patterns. Electron density of simulations like (3ad9664..., see tab. D)

The presented rough calculations mainly show the available power ready for conversion and should be understood as a rule of thumb. Since they do not proof explicitly that a coherent process is actually happening, there is yet more to understand in sense of coupling of both processes and inter-area coupling of every process itself. Simulations as depicted in fig.4.2 motivate the possibility of radiation triggered maser-like activity which then would have a radiative output on the scales of our estimation, (4.9),(4.14). A cone like structure similar to that of the simulation of $n_{rad} = n_o$ is much more likely to amplify radiation coherently. Furthermore to determine real radiative output of such patterns one would need to model the field configuration in much more detail and investigate the propagation of this radiation through the magnetosphere.

The exact mechanism that irradiates this immense power is yet to be determined, but we've succeeded in showing that the two stream instability is a viable framework to provide structured patterns of size, strength and free energy to drive coherent radio emission on the scales we observe with radio telescopes. First steps towards an examination of the output mechanism already show a promising Fourier transformation, done for the E_z field outside the active current's area (see fig. 4.3) especially when compared to typical observed nanostructure frequency dependencies (see section 1.4 and fig. 1.4) and thus should motivate further investigation.

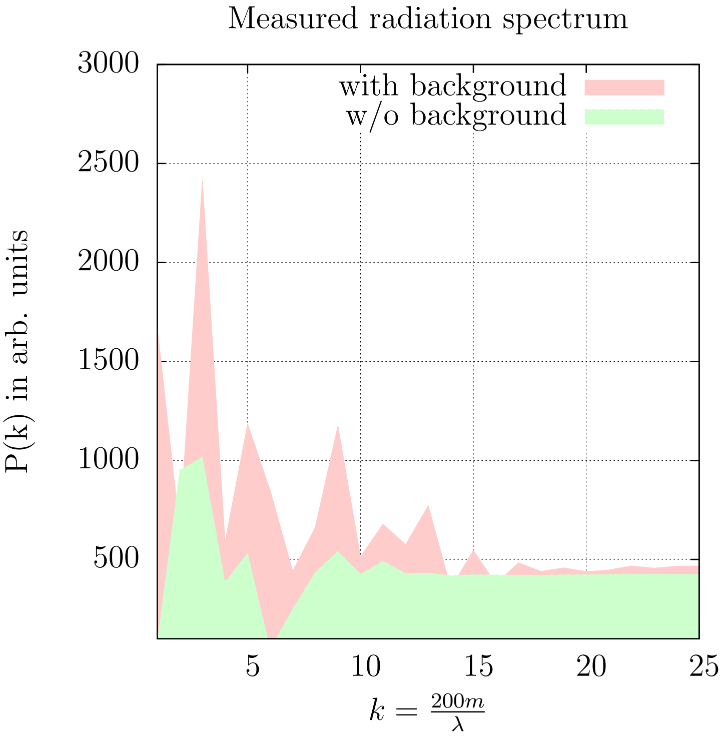

Figure 4.3.: The Fourier transformation of E_z field clearly shows peaks for radiation of the first kind, compare with fig. 1.4

5. Results

> Summoning his cosmic powers
> And glowing slightly from his toes
> His psychic emanations fly
> *'Let there be more light' by Pink Floyd*

5.1. What has been done

Introducing the reader to the observational data gained from pulsars we motivated main criteria on possible radio emission processes (see sec. 1.6) and explained the structure of the thesis.
Proceeding, we have focussed our analysis on the relativistic two stream instability and derived the proper dispersion relation for equally dense positron and electron beams counterstreaming with velocity v_o and γ_o for every species. The derived relation(2.10) was found to be in accordance with transformed versions common in literature. We studied the relation in numerical simulations for cross validation of both theory and code (fig 2.5). The appearance of white noise for a higher resolution drew our attention to what first looked like a numerical instability. Detailed analysis however revealed that the TSI cannot develop a characteristic scale when it is not properly excited or damped because it's fast development as an instability of the potential renders such an evolution impossible. We found good agreement of development with the carefully applied linear analysis (understanding the limits of linearity) and could reproduce the time and spatial lengthscales derived from theory. The TSI turns out to develop over only a few plasma cycles and wavelengths. Numerically we studied the beginning of the nonlinear phase (sec. 2.6) and gained knowledge on how possible radiation processes could come about. By the phasespace analysis it came clear that the TSI's late phase consists of bunched slabs crossing each other rather independently and that in this phase, the common plasma approximations break down. The plasma is highly structured in configuration space on the scale of the instability leading to a maximum of possible polarization on the characteristic wavelength. This concludes the main evidence why the plasma instability could drive or be (in late stage) a process obeying criteria one to three (see sec. 1.6), namely coherence, small accommodation and (secondary) strong bursts on short scale. As the TSI was found to be quite strong and an electron positron counterflow in an electric field seems natural. Thus constraint six, ubiquity, seemed also to be fulfilled at that time. Since the big variance of plasma frequency would even lead to ubiquity of the

TSI everywhere in a single atmosphere, we examined the influence of an electric field on the instability to understand whether the growth is possible everywhere. Two main influences of an electric field were discussed. On one hand, the stretching of density configurations by an electric field prohibited the instability for momenta and γ-factors of the input lower than a certain $\gamma_{\max}$ as a function of the electric field. On the other hand, we found that a gain of inertia due to gain of energy by passing the electric field leads to a shift of the resonant wavelength and will, if it happens to fast, inhibit the growth of the TSI. Leaving aside possible resonances, both requirements impose strong restrictions on the occurrence in a pulsar magnetosphere, as described in section 3.5. Deriving approximations on the minimal radii at which the TSI may happen in an individual pulsars magnetosphere, we find astonishing agreements with common observational data, suggesting the radio output to appear in the hundred MHz to GHz region (from a length scale on the order of cm to m). However the model partly may fail for millisecond pulsars since the derived radius is bigger than the light cylinder for this population. Since the model only fails by one magnitude[1] this could be accounted to a possibly better shielding of the closed field lines' electric field by the plasma current of the open field lines. Also simulations have shown(see fig. 4.2) that the instability may develop with outer electric fields way stronger than $\gamma_{\max}$ suggests.

An estimation of the possible coherent radiation output suggests that the TSI may, if the final radiation process will have enough free energy, account for the radio luminosities observed. Furthermore, interesting frequency structures arose also seen in some papers about the nanosecond shots.

Having dealt with the analytic calculations and numerical simulations, the two stream instability turns out not only to be an ubiquitous but also a fast and strong configuration space structuring process. Its length and timescales fit those of the radiation observed up to a magnitude and less. The presented arguments on a very general level together with the carried out numerical studies thus show strong evidence of the instability happening in a real pulsar magnetosphere.

5.2. What should be done

However the author suggest that a lot of details in this concept study need further investigation. The common critique[MG99] that instability driven amplification of e.g. Langmuirwaves is not strong enough may be opposed by shifting the understanding of instabilities not as the amplifier of radiation but the very driver on a local short scale. A $k_{\max}$ (2.18) could at low γ-factors perhaps even exceed the plasma frequency leading to light mode propagation. Cyclotron resonance and various propagation effects could perhaps change this picture. One should therefore exactly study

---

[1] The magnitude of the longer period pulsars radii also seem to miss observations by about a magnitude

the possible radiation processes being driven and, as a second issue, see how they couple with the pulsar magnetosphere. In principle, this investigation could lead to an acceptable pulse shape model when combined with a regeneration time analysis for the instability and the origin of the emission region determined by deepening of the methods introduced in this thesis. To that extent, one should further investigate the potential gradients tolerated by the instability and the possibly induced electric resistance. Overall pulsar simulations like those carried out by Kalapotharakos et al.[KKHC12] on one hand could greatly benefit from induced resistance and flow studies, on the other their data will be helpful in determining realistic assumptions on the E-field gradient beyond the Goldreich-Julian model. Putting both these aspects together will perhaps finally lead to a decision whether or not the TSI is the cause or one of the causes for radio radiation.
Furthermore, another limit on growth of the TSI could possibly also be calculated: When the electric field becomes too weak, the instability is not any more damped enough to show its characteristic frequency, just as seen in the high resolution limit of the simulations lacking an electric field. This would amount to a $r_{\max}$ for radio radiation output. Surely one should give concept studies on the appearance in certain well examined pulsars bigger weight, but we merely want to state here that there is also another lower limit to the instability further restricting the emission region.

5.3. What remains to be said

Today's available computing power may give many hints beyond analytics alone and their results can be seen as guiding the analytical framework into the right directions. The argumentation featured here greatly profited from the interplay between both methods. Computational methods and power may have at some time in the near future reached a level where the problem of radio radiation may be solved in that way.

The simulations presented show that, against common opinion, the two stream instability may exist and be powerful in magnetospheres. However, like all other proposed emission processes, it would have to pass the barrier of the magnetosphere. If future investigation of the power output and magnetosphere propagation would show that its flux is strong enough, the two stream instability will probably provide a framework with few free parameters and physics only dictating the length scale.
These steps shown, the TSI would naturally and in a simple way fulfil the constraints on a pulsar radio emission process.

It is this light in the distance, which urges us to continue research on the topic.

A. Derivations

A.1. Brightness temperature approximation

The radiated power per area by a black body is calculated by integrating Planck's formula for the radiation density:

$$P_\nu(T) = \int \mathrm{d}\nu \frac{2h\nu^3}{c^2(\exp[\frac{h\nu}{k_B T}] - 1)} \tag{A.1}$$

For a small frequency band we may approximate the integration by multiplication with the bandwidth. We set this equal to the observed power output in the band divided by the radiating surface.

$$P_\nu(T) \approx \frac{2h\nu^3}{c^2(\exp[\frac{h\nu}{k_B T}] - 1)} \Delta\nu \approx \frac{L_\nu}{A} \tag{A.2}$$

solving this for $h\nu/(k_B T)$ and approximating for $h\nu \ll k_B T$ yields:

$$\frac{h\nu}{k_B T} = \ln\left[\frac{2h\nu^3 \Delta\nu A}{c^2 L_\nu} + 1\right] \approx \frac{2h\nu^3 \Delta\nu A}{c^2 L_\nu} \tag{A.3}$$

finally we arrive at the desired formula

$$T_{bb} \approx \frac{L_\nu c^2}{2A\Delta\nu\nu^2 k_B} \tag{A.4}$$

A.2. Larmor's formula in terms of an external potential

The relativistic generalization to Larmor's formula can be found if not derived directly e.g. in [RK10].

$$\langle P_{\mathrm{single}} \rangle = \frac{1}{T} \int_0^T \mathrm{d}t \frac{2e^2}{3m^2c^3} \left| \frac{\mathrm{d}p^\mu}{\mathrm{d}\tau} \right|^2 \tag{A.5}$$

We again may derive relativistic equations of motions for a single particle by contracting the four momentum vector and setting it to the invariant rest mass of the particle.

$$p^{\mu} = \begin{pmatrix} \frac{1}{c}\Phi(x) \\ \vec{p} \end{pmatrix} = \begin{pmatrix} \frac{1}{c}\Phi(x) \\ \sqrt{\frac{1}{c^2}\Phi^2(x) - (mc)^2} \end{pmatrix} \tag{A.6}$$

Deriving this with respect to the eigenzeit we find:

$$\frac{\mathrm{d}p^{\mu}}{d\tau} = \left(\frac{\frac{1}{c}\partial\Phi(x)}{\partial x}\frac{\partial x}{\partial t}\frac{\partial t}{\partial \tau}, \frac{\frac{1}{c}\Phi(x)\frac{\partial \frac{1}{c}\Phi(x)}{\partial x}\frac{\partial x}{\partial t}\frac{\partial t}{\partial \tau}}{\sqrt{\frac{1}{c^2}\Phi^2(x) - (mc)^2}} \right) \tag{A.7}$$

where we've reduced the solution to 1 spatial dimension as it is the case in our problem. Contracting this expression with itself leads to

$$\begin{aligned} \dot{p}^{\mu}\dot{p}_{\mu} = & \left(\frac{\frac{1}{c}\partial\Phi(x)}{\partial x}\frac{\partial x}{\partial t}\frac{\partial t}{\partial \tau} \right)^2 \left(\frac{\frac{1}{c^2}\Phi^2 - (mc)^2 - \frac{1}{c^2}\Phi^2}{\frac{1}{c^2}\Phi^2 - (mc)^2} \right) = \\ = & \left(\frac{\frac{1}{c}\partial\Phi(x)}{\partial x}\underbrace{\frac{\partial x}{\partial t}\frac{\partial t}{\partial \tau}}_{v_o\gamma} \right)^2 \frac{1}{1 - \underbrace{\frac{\frac{1}{c^2}\Phi^2}{(mc)^2}}_{\gamma^2}} = \\ = & \left(\frac{\frac{1}{c}\partial\Phi(x)}{\partial x} \right)^2 \frac{v_0^2\gamma^2}{1-\gamma^2} = \left(\frac{\partial\Phi(x)}{\partial x} \right)^2 \end{aligned} \tag{A.8}$$

where we've used that $v_o = \sqrt{(1-\gamma^2)/\gamma^2}c$. Thus we can write

$$\langle P_{\text{single}} \rangle = \frac{1}{T}\int_0^T \mathrm{d}t \frac{2e^2}{3m^2c^3}\left(\frac{\partial\Phi(x)}{\partial x} \right)^2 = \frac{2e^2}{3m^2c^3}\langle\left(\frac{\partial\Phi(x)}{\partial x} \right)^2\rangle \tag{A.9}$$

For relativistic particles, the average may be taken over space since $\beta \approx 1$ over the whole interval. Thus, in the limit of high γ, the form of the potential alone determines the energy loss.

B. Numerical Methods

B.1. The Plasma Simulation Code

We used the Plasma Simulation Code, in the following abbreviated by *PSC* extensively for the simulations contained in this thesis. The PSC is a relativistic particle in cell(=PIC) code. It's original code base was written by Hartmut Ruhl in Fortran and is now integrated and ported into a bigger framework written in C by H. Ruhl and his chair along with Kai Germanschewski of the University of New Hampshire. The complete list of contributors may be retrieved via the git version control system. The Code itself is designed to scale well on large cluster systems and the framework is written modular to be easily extendible. The code undergoes heavy development at the time of writing this thesis. For example the UPML boundary conditions(explained in section B.2.1) are considered to be stable now at the end of the thesis but had issues during the making of the simulations, so we dropped use of them for this thesis. The code will in near future be able to do adaptive mesh refinement, adaptive particle refinement and QED-reactions, all techniques required for realistic larger scale simulations of a pulsar magnetosphere. There's a plethora of features like Cuda[1] support already implemented or coming up soon. By now the framework's API itself is documented via sample case setups and a DoxyGen documentation coming along with the code. We will refrain from giving an introduction to the code. Instead we will summarize the most important theoretical concepts in the next section. The subsequent sections will give insights to our specific case's setup and explain what has been done to elaborate the specific code for setting up the simulations presented.

There are already excellent introdutions to the theoretical workings of the code around, e.g. [Mos11, Ruh] the following considerations are based on. Thus we will focus our attention on only two aspects of the code, namely the Yee-algorithm for solving Maxwell's equations and discretization of the Vlasov equations for particle dynamics. Understanding both at least on a basic level is vital to interpreting our simulation outcome.

---

[1] API for doing calculations on the GPU of a computer's graphics card

B.1.1. The Yee algorithm

The Yee algorithm[Yee66] is an algorithm to solve Maxwell's equations by imposing a finite difference time domain (FDTD) scheme on a staggered grid discretization of the electromagnetic field. A straight forward discretization of Maxwell's equations replaces the continuous fields by values on a grid, and derivatives are approximated after the classical second order scheme:

$$\vec{F}(\vec{x},t) \rightarrow F^{t}_{x,y,z} \tag{B.1}$$

$$\nabla F(x,t) \rightarrow \frac{F^{t}_{x+\frac{1}{2},y,z} - F^{t}_{x-\frac{1}{2},y,z}}{\Delta x} \tag{B.2}$$

$$\frac{\mathrm{d}F}{\mathrm{d}t} \rightarrow \frac{F^{t+\frac{1}{2}}_{x,y,z} - F^{t-\frac{1}{2}}_{x,y,z}}{\Delta t} \tag{B.3}$$

Where t, x, y, and z are now of discrete nature. Applying this kind of discretization to Maxwell's equations in dimensionless form leads to discrete equations with two shifted forms of the differential operator:

$$\partial t\vec{E} = \vec{\nabla} \times \vec{B} - \vec{j} \qquad \rightarrow \qquad \frac{\vec{E}^{n+\frac{1}{2}}_{jkl} - \vec{E}^{n-\frac{1}{2}}_{jkl}}{\Delta t} = \vec{\nabla}^{-} \times \vec{B}^{n}_{jkl} - \vec{j}^{n}_{jkl} \tag{B.4}$$

$$\partial t\vec{B} = -\vec{\nabla} \times \vec{E} \qquad \rightarrow \qquad \frac{\vec{B}^{n+1}_{jkl} - \vec{B}^{n}_{jkl}}{\Delta t} = -\vec{\nabla}^{+} \times \vec{E}^{n+\frac{1}{2}}_{jkl} \tag{B.5}$$

$$\partial t\rho = -\vec{\nabla}\vec{j} \qquad \rightarrow \qquad \frac{\rho^{n+\frac{3}{2}}_{jkl} - \vec{\rho}^{n+\frac{1}{2}}_{jkl}}{\Delta t} = \vec{\nabla}^{-} \cdot \vec{j}^{n+1}_{jkl} \tag{B.6}$$

where $\vec{E}$ denotes the electric, $\vec{B}$ the magnetic field, $\vec{j}$ is the current and ρ the charge density. All quantities shown are normalized as indicated in appendix C. The left/right weighted operations of the differential operator are:

$$\begin{aligned}
\vec{\nabla}_{-}F^{n}_{jkl} &= \left(\frac{F^{n}_{jkl} - F^{n}_{j-1kl}}{\Delta x}, \frac{F^{n}_{jkl} - F^{n}_{jk-1l}}{\Delta x}, \frac{F^{n}_{jkl} - F^{n}_{jkl-1}}{\Delta x}\right) \\
\vec{\nabla}_{+}F^{n}_{jkl} &= \left(\frac{F^{n}_{j+1kl} - F^{n}_{jkl}}{\Delta x}, \frac{F^{n}_{jk+1l} - F^{n}_{jkl}}{\Delta x}, \frac{F^{n}_{jkl+1} - F^{n}_{jkl}}{\Delta x}\right)
\end{aligned} \tag{B.7}$$

The resulting derivation infinitesimally equals the Maxwell's equation. One could have obtained it from considering electromagnetism in terms of differential forms. In the framework of forms it comes obvious that we basically apply Stoke's theorem to the field values around an elementary cell(See also [MTW73],chapter 4). These considerations naturally lead to the so called staggered grid the PSC is set up with. Electric and magnetic fields are neither defined at the same time nor their components at the same space point. They are shifted to the exact positions determined by

Stoke's theorem on a cube and considerations about the temporal integrations.

$$\vec{E}^{n+\frac{1}{2}}_{jkl} = \left((E_x)^{n+\frac{1}{2}}_{j+\frac{1}{2}kl}, (E_y)^{n+\frac{1}{2}}_{jk+\frac{1}{2}l}, (E_z)^{n+\frac{1}{2}}_{jkl+\frac{1}{2}} \right) \tag{B.8}$$

$$\vec{E}^{n}_{jkl} = \left((B_x)^{n}_{jk+\frac{1}{2}l+\frac{1}{2}}, (B_y)^{n}_{j+\frac{1}{2}kl+\frac{1}{2}}, (B_z)^{n}_{j+\frac{1}{2}k+\frac{1}{2}l} \right) \tag{B.9}$$

$$\vec{j}^{n+1}_{jkl} = \left((j_x)^{n+1}_{j+\frac{1}{2}kl}, (j_y)^{n+1}_{jk+\frac{1}{2}l}, (j_z)^{n+1}_{jkl+\frac{1}{2}} \right) \tag{B.10}$$

Since it only infinitesimally equals Maxwell's equation our second order approximation naturally produces errors. But also the exact solutions to this equations change. Where we have a dispersion relation in vacuo of $\omega = ck$ these is not true for our discrete grid. When setting up elementary amplitudes the form of an exponential with phase of $\omega t - \vec{k}\vec{x}$ we do find a dispersion relation preferring the axis directions and with group velocity slower than c for high frequencies. Considering the one dimensional case, if $\frac{\Delta t}{\Delta x} \cdot < 1$ (in dimensional quantities) is violated we find exponentially growing wave solutions and our algorithm becomes unstable. Thus a certain 3d-type of this so called CFL-Condition (named after Courant, Friedrichs and Lewy, [CFL28]) has to be fulfilled[2]. The factor on the lhs of the condition in fact should be considerably smaller than one since the dispersion relation only approximates the continuum solution and the approximation gets better for a smaller factor. Since dispersion relations do not match, discrete waves of high frequency have a lower speed of light. Thus a seemingly faster than light particle evokes Cherenkow radiation. This means, that when doing relativistic particle simulations, one is obliged to keep this coefficient low enough to prevent superluminosity, resulting in the computational cost of more timesteps. However, vacuum Cherenkow radiation arises only in situations where the integrated current of a plasma has profile structures near the spatial scale of the grid that propagate faster than light. This is typically not the situation in our case, especially not in the linear phase of the TSI.

In this discrete version of Maxwell's equation, we only update the electromagnetic field according to the current. Thus, we have to take care of setting up a physically correct electric and magnetic field also fulfilling div$\vec{B} = 0$ and Poisson's equation as an initial condition. Correct electro- and magnetostatics come by initial condition, and are not enforced by the code itself.

B.1.2. Vlasov equation and the quasiparticle approach

The discretized version of Maxwell's equation now is coupled to a plasma of particles. The Vlasov-Maxwell system of equations provide a way to implement this coupling. Discretization of both particles and fields is not straightforward since solving an N-particle problem naively means solving the 6N coupled equations of motion for positions and momenta. For typical particle numbers of lots of trillions, solving the system directly will certainly not become computationally feasible. This classical problem is tackled by noticing that we are generally interested in statistical answers since typically N is very large. As such, we may relax our requirement to describe all N particles by using a statistical approach upon which we try to model the behaviour of the system. Rather than setting up a 6N-dimensional phasespace vector we define a distribution function $f(\vec{x}, \vec{p}, t)$ for every kind of particle which states the probability to find such a particle in an infinitesimal phasespace volume element. Since description of initial conditions in plasma physics follows this ansatz (e.g. "Let us take a plasma of density n and temperature T) we automatically adapt a framework in which the questions asked may be deduced from our arising distributions and possibly their correlations. We're not interested in a single outcome but a typical behaviour of the system[3] and can extract that behaviour easily from the dynamics of the distribution function(s).

---

[2] The Code ensures this to be fulfilled throughout the simulation

Arriving at such a formalism leads from the n-particle equations of motion over Liouville's equation to the BBGKY-Hierarchy. A thorough analysis can be found e.g. in Cergignani,[Cer69]. Let us review the main results therein:

Collective phenomena can be described by assuming independence of single phasespace element w.r.t. then effectively external forces. However, local interactions such as collisions typically need correlated distribution functions like the two particle function $f_2(\vec{x}_1, \vec{p}_1, \vec{x}_2, \vec{p}_2, t)$ being proportional to the probability of finding two particles in two certain phasespace volumes. This is to regard the fact that there ought to be two particles in certain distinct phasespace volumes for a certain type of collision to happen. In general transforming the Liouville equation leads to a hierarchy of equations coupling N-particle distribution functions to N+1-particle distribution functions, namely the BBGKY-hierarchy. If the given higher distribution functions are mostly zero, we may separate these correlation terms and treat them separately as collision operators. Furthermore we may under certain conditions break the hierarchy and for large N approximate e.g. $f_2(\vec{x}_1, \vec{x}_2, \vec{p}_1, \vec{p}_2) \approx f_1(\vec{x}_1, \vec{p}_1, t) f_1(\vec{x}_2, \vec{p}_2, t)$. One may motivate that if collision terms only play a role for very short periods of time and are generally symmetric w.r.t. particle exchange. Thus they will yield independent outcomes for each collision since the particle propagation on larger scales mixes initial conditions to a single collision quasi independently. This behaviour is in general not trivial to show.

Luckily the short range interaction between two particles can be separated in the so called Boltzmann Collision Operator, which at our densities does not even play a role for physics. We're left with a Boltzmann-Vlasov type of equation for the single particle distribution function, where only the collective field of all the particles contributes. The coupled 6N equations (for particles alone) essentially decouple into Maxwell's equations for the fields and a distribution function equation for particle behaviour. We may integrate them interleaved under the assumption that both do not change rapidly in time.

The PSC's representation of the one particle distribution function is a sum over quasiparticles that are δ-distributed in momentum space and have a diamond shaped form factor in position space.

---

[3] And that is what we'll always yield at such particle numbers

$$f_k(\vec{x},\vec{p},t) = \frac{\alpha^2 M^3}{\eta m_k^3 N_c} \sum_{i=0}^{N_k} \Phi(\vec{x},\vec{x}_i^k(t))\delta^3(\vec{p}-\vec{p}_i^k(t)) \tag{B.11}$$

$$\Phi(\vec{x},\vec{x}_i^k(t)) = \prod_{j=1}^{3} S_j(xj, x_{ij}^k(t)) \tag{B.12}$$

$$S_j(x_j, x_{ij}^k(t)) = \begin{cases} 1-\left|\frac{x_j-x_{ij}^k}{\Delta x_j}\right| & \text{for } x_{ij}^k-\Delta x_j < x_j < \Delta x_j + x_{ij}^k \\ 0 \text{ elsewhere} \end{cases} \tag{B.13}$$

The normalization factors introduced here are described in section C. In general, a single quasiparticle stands for a typical distribution of lots of real particles. We emphasize that it is a distribution function which essentially behaves like a particle density, but is conceptually different from a swarm of particles since it is part of a distribution. There is no straightforward equivalent of a test-particle in the PSC. Automatically arising with this formalism is the interpolation of field values, since a quasiparticle has an extent of two grid units in every dimension and thus extents to several cells. Inserting these phasespace quasiparticles into the Vlasov equation(2.2)

$$\partial_t \int \mathrm{d}^3 v \vec{v} f_k + \partial_{x_l} \int \mathrm{d}^3 v v_l \vec{v} f_k - \int \mathrm{d}^3 v \partial_{v_l} \left(\frac{q}{m}\left[\vec{E}+\vec{v}\times\vec{B}\right]_l \vec{v}\right) f_k = 0 \tag{B.14}$$

$$\sum_{i=0}^{N_k} \left(\dot{\vec{x}}_i \cdot \partial_{\vec{x}_i} \Phi(\vec{x},\vec{x}_i) + \vec{v}_i \cdot \Phi(\vec{x},\vec{x}_i)\right) \cdot \vec{v}_i + \sum_{i=0}^{N_k} (\dot{\vec{v}}_i - \underbrace{\frac{q}{m}\left[\vec{E}+\vec{v}\times\vec{B}\right]}_{=:\vec{F}(\vec{x},t)})\Phi(\vec{x},\vec{x}_i) = 0 \tag{B.15}$$

and integrating over momentum and a single cell volume yields effective equations of motion for every quasiparticle's coordinates:

$$\frac{\mathrm{d}\vec{x}_i}{\mathrm{d}t} = \vec{v}_i \tag{B.16}$$

$$\frac{\mathrm{d}\vec{v}_i}{\mathrm{d}t} = \frac{1}{\prod_{l=1}^{3} \Delta x_l} \int \mathrm{d}^3 x \Phi\left(\vec{x}-\vec{x}_i\right) \vec{F}(\vec{x},t) \tag{B.17}$$

That is why the method is called PIC, particle in cell. It should not come as a surprise that we find Newtonian equations of motion for every quasiparticles position and momentum as an approximation (see [Ruh] p. 25). However let us stress again that nevertheless the concept and meaning of a quasiparticle is different from a real particle.

Quasiparticles in general have very convenient properties. As they are stretched in position space, they may not pick up high frequencies in force terms and naturally provide a smooth current to use on the grid. Furthermore the diamond sized shape is ideal to model constant initial densities by setting them up on distances according to their half extension. The relativistic version of this is obtained straightforward and implemented in the PSC code.

B.2. Simbox setup

Whilst the used PSC-code already comes self consistent, setting up correct physical initial conditions is an equally important ingredient to a confident simulation. This turns out to be more cumbersome than at the first glimpse for several reasons.
First of all, any analytical solution on continuous space has to be discretized. The solution in continuous reality does not exactly match the one on a discretized grid. However choosing appropriate continuous initial conditions and discretizing this solution carefully using techniques like those described below reduces the numerical errors of the initial setup to an acceptable degree.
But we have to deal not only with the finite resolution of our grid but also with the finite domain our simulation takes place in. Choosing appropiate boundary conditions at the borders of our simbox is also a tedious task. Since excess space is expensive in calculations, we need to limit it to a minimum. Consequently the boundary is somewhere near the area of interest and might influence the events we want to observe. E.g. choosing a conducting boundary means we will have to fulfil appropriate boundary conditions. This, owing to continuity and smoothness leads to different fields inside the simbox. Thus some desired field geometry in space might not be compatible with every boundary condition or is subject to bigger modifications to cope with the choice of boundary conditions.
In general we have an exact notion of what we want to simulate or measure in mind. Just like an experimentalist we now have to come up with a modified setup of what would be the scenario in theory and make the right choices regarding the initial setup. We have to be aware that most of these choices also modify the outcome of the simulations and gain an understanding of the influence they take to interpret our results correctly.

B.2.1. Choosing geometry and boundary conditions

All of the simulations presented investigate two stream instabilities with a counterstreaming electron and positron flow. While it is a neutral current yielding no electrical field, we yield a net current. But with a net current comes a magnetic field which already would extend to the boundaries. The main four boundary types and their advantages and drawbacks are:

- *Open Boundaries:* The boundary essentially behaves like a perfect conductor. Thus, the parallel E-fields always yield zero. Since we later on want to simulate the current being influenced by an paraxial electric field, this type of boundary causes problems

- *Conducting boundaries:* The boundary is a conductor with a resistance and susceptibility. Our electric field would also be diminished, which is not feasible.

- *UPMLS, uni-axial perfectly matched layers:* The boundaries absorb emitted radiation up to a very small, reflected part. This boundary conditions are useful for measuring radiation outflow and have been taken into consideration. However their workings are complex and interspersing them with constant fields like the guiding background field of our simulations would have needed further investigations to ensure proper functionality. Further technical difficulties lead to the initial design choice of implementing the fourth basic type, periodic boundaries. An additional drawback might be that these boundaries are thick meaning they occupy a few grid cells at each boarder and need additional calculations to be made.

- *Periodic boundaries:* Space is wrapped up like a torus embedded in four dimensions. While we can consider this setup to be globally unphysical, locally it is as one would have no boundary at all since all waves and particles pass the boundary and enter the simbox again on the opposite site. Periodic boundaries demand the initial field values to be also periodic and continuous. Furthermore they have a discrete eigenmode spectrum leading to filtering effects in long-time (timesteps > gridlengths) simulations. Once having fulfilled the initial conditions they are a fast and good choice since their effect is clear and they do not modify small scale field structure.

As an initial setup we decided for the periodic boundaries. The only problem we have to solve to implement our theoretical setup, a neutral current, is its non vanishing magnetic field. Since $\mathrm{rot}\vec{B} \propto \vec{j}$ we yield for a current simply moving in z-direction $\vec{B} \propto (-x, y, 0)$. Thus the B-field is periodic, but not continuous at the borders. To fix we shield the current's magnetic field by an artificial static current hull. To simplify calculations, we choose a round geometry as depicted in fig.B.1. We set up a cylindric current surrounded by a pseudocurrent shielding the magnetic field. In this configuration, one is able to fulfil the requirements. But let us first start with deriving the analytical solution of this rather simple setup.

B.2.2. Determining and setting initial field and currents

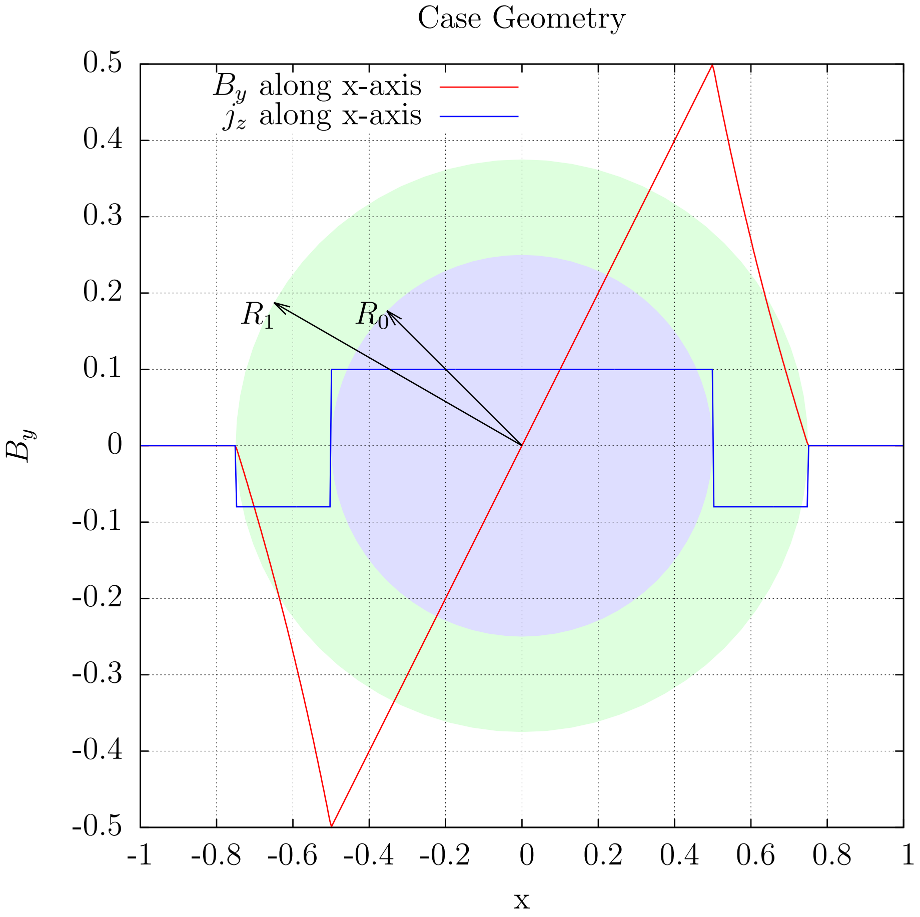

Figure B.1.: Concept of case setup, cut through x-y-plane of simbox. Depicted in light blue is the current due to the real quasiparticles. The instability can only happen in the central region. The magnetic field created by the current is shielded by a pseudocurrent hull, depicted in green. This is an artificial, static current as if it was created by charged particles not subject to the Lorentz force. The overlayed plot displays values of currents and magnetic fields along the x axis. The decay line of the magnetic field in the shielding current region is nonlinear, see text.

The current density in the middle of the cylinder, j_0 is a function of the quasiparticle density n_0 and the initial velocity, v_0 and constant in the interior and hull, respectively. We demand the Magnetic field's rotation to vanish outside our cylinder. By the law of induction and using Stokes' theorem, we conclude that the net current enclosed in the cylinder has to vanish. This leads to the condition that

$$-R_o^2 \pi j_o = (R_1^2 - R_0^2) \pi j_1 \tag{B.18}$$

where j_1 is the current density of the hull. Let us define the hull to be $\frac{1}{d}R_0$ thick, thus $R_1 = (1+\frac{1}{d})R_0$ and we yield

$$\begin{aligned} -R_o^2 \pi j_o &= ((1+\frac{1}{d})^2 - 1) R_o^2 \pi j_1 \\ j_1 &= -\frac{d^2}{1+2d} j_0 \end{aligned} \tag{B.19}$$

Leaving aside the constant B-field background in z-direction, we now want to calculate the B-field in the x-y-plane. The problem is symmetric in z-direction and circular symmetric around the z-axis. Thus we expect the current to have a B-field dependent on r in e_ϕ direction. Using Stokes' theorem with circles centred at the origin we find

$$\int \mathrm{d}\phi B_\phi(r) = \begin{cases} \frac{4\pi}{c} \int_{A:=\{x^2+y^2<r\}} j_0 \mathrm{d}A & \text{for } r \leq R_0 \\ \frac{4\pi}{c} (j_o \pi R_0^2 + \int_{A:=\{R_0<x^2+y^2<r\}} j_1 \mathrm{d}A) & \text{for } R_0 < r < R_1 \\ 0 & \text{elsewhere} \end{cases} \tag{B.20}$$

$$2\pi r B_\phi(r) = \begin{cases} \frac{4\pi^2}{c} r^2 j_0 \mathrm{d}A & \text{for } r \leq R_0 \\ \frac{4\pi^2}{c} \left(R_0^2 j_0 + (r^2 - R_0^2)\, j_1\right) & \text{for } R_0 < r < R_1 \\ 0 & \text{elsewhere} \end{cases}$$

$$B_\phi(r) = \begin{cases} \frac{2\pi}{c} r j_0 & \text{for } r \leq R_0 \\ \frac{2\pi}{c} \frac{R_0^2}{r} \left(j_0 + \left(\frac{r^2}{R_0^2} - 1\right) j_1\right) & \text{for } R_0 < r < R_1 \\ 0 & \text{elsewhere} \end{cases} \tag{B.21}$$

Note that while the B-field values rise linearly in the real current region, the shielding pseudocurrent not subject to Lorentz's force decays nonlinear with radius. Typically, we want our simbox to be a few hundred cells in height and width containing a rather large active current area in the middle and a small pseudocurrent hull. Since the continuous formulae of currents(B.19) and magnetic fields(B.21) are used to initialize a finite grid, a common sampling error occurs named *aliasing*. These errors are the natural consequence of using conditions with greater or equal signs or Θ-functions. A circle, to give an example, is badly represented by the condition "mark every spot $(x,y); x,y \in \mathbb{N}$ that fulfils $x^2+y^2 \leq R^2$ ". This gives a bad sampling for values of x and y that nearly fulfil the condition, see figure B.2. An easy and appropriate fix in our situation is to interpolate the function's values linearly over one grid cell around the radii. The computational error introduced by that is way smaller than the error introduced by aliasing.

Furthermore we have to deal with the code being executed on a staggered grid. This means that the analytical solution to the Maxwell's equation are subject to an in general tiny correction. This correction has been made experimentally in the following way: One can set up the initial conditions on a grid with small z-length. On such a grid, lateral instabilities of the beam cannot develop. The simulation

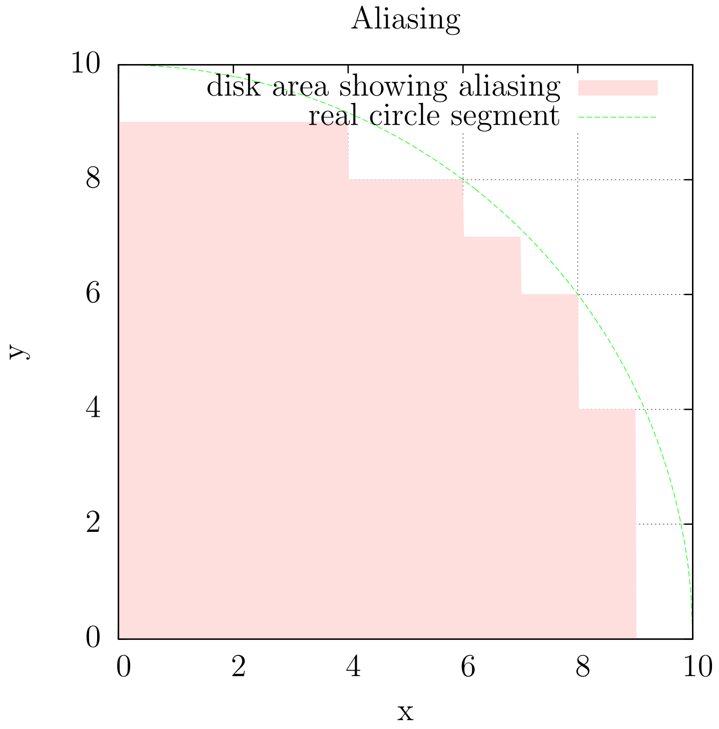

Figure B.2.: When discretising continuous formulae, Θ-functions have to be interpolated to avoid aliasing. E.g. simply checking if $r < R_0$ holds gives large numerical errors leading to a non accurate setup.

should not build up an E_z field after a few steps of computation unless one sets the currents wrong. However one always introduces an error. Two criteria are to be met before proceeding with a full simulation:

1. The error building up E_z should remain small compared to the field that would be built up if no B-field was present
2. The artefacts at the hull's borders should be small compared to the field that would be built up if no B-field was present

We met criterion one at about 10^{-4}, criterion two at about 10^{-1}. It is only then the instabilities can develop as derived.

B.2.3. Modifying the setup to maintain a quasi constant E_z field

To test the workings of the TSI in an electric field, one wants to modify the above setup to include a constant E_z field. This would mean to solve Maxwell's equations for $\partial_t E \overset{!}{=} 0$ leading to some Bessel functions[4] forming a smooth dip of the field in the middle and according bumps at the quasicurrent's site. We omit that peculiarity since it anyway sets our field configuration nonconstant along the transversal axis. Instead we just compensate for the additional charge flux of the real current by putting a uniform growing pseudocurrent in the middle cylinder. This is done without much care by solving

---

[4] Bessel functions arise because the Laplace operator on the l.h.s. of Maxwell's equations has to be solved for a j on the r.h.s. dependent on E

$$\begin{aligned} \dot{p} &= \frac{Ee}{mc} \\ p &= \frac{Ee}{mc}\Delta t + p_0 \end{aligned} \tag{B.22}$$

and adjusting the pseudocurrent's strength after this formula. In reality the fields could be dominated by the closed field lines' charged cargo and the field drop could form a broader valley of nearly constant E_z in the middle. However simulation limitations in both size and density currently restrict us to the regime where we have to suppress the development of a transversal electric field gradient. Strictly speaking we break self consistency in transversal direction to the benefit of easier analysis of the outcome. The newly added pseudocurrent keeps E_z constant along the transversal axes and inhibits the growth of the magnetic field rot$\vec{B} \propto \vec{j}_z$. Meanwhile it leaves the important properties of the system, namely momenta, difference fields and positions intact.

One caveat is that we're by now actively pumping energy into the system. This has to be taken into consideration when measuring anything related to energy.

B.3. Integrating E_z to gain a notion of potential

For the potential plot in fig. 2.6 one needs to define what a potential is. In our case we reduce the problem to one dimension, meaning we omit the arising rotation in the x and y components of the E-field and average the E_z component over x-y-slices. Then, the average E_z-field is collected and integrated to gain the potential. This potential is then linearly transformed to get rid of eventually built up net electric fields and to remove bias. Thus the local potential differences the instability consists of remain. We expect the potential to be symmetric under point reflection since the whole setup itself is point symmetric under charge transformation.

C. Normalization

We use Gaussian CGS-units and formula where not otherwise stated. However some numerical values are given in SI units where appropriate.
The PSC partly lets you choose your favourite system of units in terms of the numerical value of nature's constants c, e, ϵ_0 and so on. However, since it is also meant to be a code capable of high intense laser plasma physics, quantities are typically normalized w.r.t. laser physics, namely the laser frequency ω. The choice of ω does not change our simulation physically but specifies 'natural units' the output is normalized to. Along with ω we define time and spatial units (these considerations are cited in slightly modified form and order from [Ruh]):

$$t \leftarrow \omega t, \qquad \vec{\lambda}_D \leftarrow \frac{\vec{c}}{\omega} \qquad \vec{x} \leftarrow \frac{\vec{x}}{\lambda_D}, \qquad \vec{p} \leftarrow \frac{\vec{p^k}}{m^k c}, \tag{C.1}$$

Where k is a sort/species index. The fields, currents and charge densities are normalized to E_0, B_0, j_0, ρ_0 defined as follows to consistently reproduce the dimensional Maxwell equations:

$$B_0 = \frac{E_0}{c}, \qquad j_o \epsilon_0 \omega E_0, \qquad \rho_0 = \epsilon_0 \omega B_0 \tag{C.2}$$

Where E_0 is a free parameter. The distribution functions f_k appearing in the Vlasov-Boltzmann description demand the following normalizations:

$$\rho_k = \frac{q^k m^{k3}}{QM^3} \int \mathrm{d}^3 p f_k, \qquad \vec{j}_k = \frac{q^k m^{k3}}{QM^3} \int \mathrm{d}^3 p, \qquad f_0 = \frac{\eta}{\alpha^2} \frac{n_0}{M^3 c^3} \tag{C.3}$$

$$\eta = \frac{v_{os}}{c}, \qquad v_{os} = \frac{QE_0}{M\omega}, \qquad \alpha = \frac{\omega_p}{\omega} \tag{C.4}$$

Where Q and M are free parameters. A convenient choice for Q is the electron charge and for M the electron mass. The "laser" frequency was sometimes set to ω_{TSI} in our case. This however does not hold for all simulations. In general, we converted all important output values from the simulation to SI / CGS units where appropriate. Momentum in the phasespace diagrams was normalized to $m_e c$.
To avoid unnecessary confusion we've only stated normalizations relevant to understand the proceedings of this thesis and remain in commonly used units, that is, for astrophysical formulae CGS, for some results SI.

D. Table of simulations

git commit (version control)	scenario	simulation
1c5ab01...	e^+ onto e^- $p = 2$ $n_0 = 6.3 \cdot 10^6 \frac{1}{cm^3}$ $20m \cdot 20m \cdot 500m$	grid $20 \cdot 20 \cdot 500$ $N_\# = 20$ boundaries periodic
d4643aa...	e^+ onto e^- $p = 2$ $n_0 = 6.3 \cdot 10^6 \frac{1}{cm^3}$ $20m \cdot 20m \cdot 500m$	grid $60 \cdot 60 \cdot 1500$ $N_\# = 20$ boundaries periodic
6d73ddb...	e^+ onto e^- $p \in \{0.3, 0.4, 0.5, 0.6, 0.7, 0.8, 0.9, 1.0\}$ $n_0 = 6.3 \cdot 10^6 \frac{1}{cm^3}$ $200m \cdot 200m \cdot 500m$	grid $100 \cdot 100 \cdot 250$ $N_\# = 5$ boundaries periodic, setting as described in section B.2
2f0c4f1...	e^+ onto e^- $p = 0.8$ $\gamma_{\max} \in \{1.2, 1.1, 1.01, 1.001\}$ $n_0 = 6.3 \cdot 10^6 \frac{1}{cm^3}$ $300m \cdot 300m \cdot 600m$	grid $100 \cdot 100 \cdot 200$ $N_\# = 5$ boundaries periodic, maintaining constant E_z field as described in section B.2.3
11181c9...	e^+ onto e^- $p =\in \{0.8, 0.458, 0.142, 0.045, 0.014\}$ $\gamma_{\max} = 1.001$ $n_0 = 6.3 \cdot 10^6 \frac{1}{cm^3}$ $300m \cdot 300m \cdot 600m$	grid $100 \cdot 100 \cdot 200$ $N_\# = 5$ boundaries periodic, maintaining constant E_z field as described in section B.2.3
440eb8b...	e^+ onto e^- $p = 1.0$ $n_0 = 6.3 \cdot 10^6 \frac{1}{cm^3}$ $20m \cdot 20m \cdot 100m$	grid $20 \cdot 20 \cdot 100$ $N_\# = 2$ boundaries periodic
3ad9664...	e^+ onto e^- $p = 1.0$ $n_0 = 6.3 \cdot 10^6 \frac{1}{cm^3}$ some different area shapes radiating electron background of $\gamma = 20$ and density of 10% or 100%n_o	grid appropriate to areas $N_\# = 5$ boundaries periodic Initial E_z field turned on

E. Used tools

In the making of this text we used the LaTeXtypesetting architecture enhanced with the pdftk toolset and TikZ graphics. For image editing we used GIMP, the GNU Image programm and Inkscape. Visualization and data analysis was done with Gnuplot and Paraview. The Fourier transforms were taken using libFFTW.
The PSC-Code as well as this document and all generating scripts were version controlled with GIT.
Development on the code was done using the GNU Compiler set and kdevelop as an IDE.
The PSC itself makes use of numerous libraries, tools and extensions including but not limited to OpenMPI, HDF5, libPAPI, SSE1/2 and Cuda, enabling parallel computing on GPUs.
The chair's cluster at the LRZ in Garching uses SUSE Linux Enterprise 11. Most of the simulations were run on behalf of this hardware. The development was done on machines running Fedora (16), a GNU/Linux distribution.
For presentational needs (the TMP program's final exam basically is a defence in form of a presentation of the master thesis) I furthermore used blender, the LaTeXbeamer architecture and mencoder.
This research has made use of NASA's Astrophysics Data System Bibliographic Services and the ATNF pulsar catalogue (see also [MHTH05]).

Bibliography

[AH00] M. P. Allen and J. E. Horvath. Pulsar radio luminosity laws revisited. *Monthly Notices of the Royal Astronomical Society*, 317:23–27, September 2000.

[BZ34] W. Baade and F. Zwicky. Remarks on Super-Novae and Cosmic Rays. *Physical Review*, 46:76–77, July 1934.

[Cam98] M. Camenzind. Neutronensterne und Pulsare, 1998.

[Cer69] C. Cercignani. *Gravitation*. Plenum Press, 2 edition, 1969.

[CFL28] R. Courant, K. Friedrichs, and H. Lewy. Über die partiellen Differenzengleichungen der mathematischen Physik. *Mathematische Annalen*, 100:32–74, 1928.

[Cha83] S. Chandrasekhar. on stars, their evolution and their stability, December 1983.

[CL02] A. R. Crusius-Waetzel and H. Lesch. Emission Mechanisms in High Energy Pulsars: From Gamma Rays to Infrared. In W. Becker, H. Lesch, and J. Trümper, editors, *Neutron Stars, Pulsars, and Supernova Remnants*, page 162, 2002.

[Fac12] Australian Telescope National Facility. ATNF pulsar catalogue 1.44. online publication, June 2012.

[GJ69] P. Goldreich and W.H. Julian. Pulsar Electrodynamics. *ApJ*, 157:869, August 1969.

[Gra99] A. Graf von und zu Hoensbroech. *The Polarization of Pulsar Radio Emission*. PhD thesis, Max-Planck-Institut für Radioastronomie, 1999.

[HBP+68] A. Hewish, S. J. Bell, J. D. H. Pilkington, P. F. Scott, and R. A. Collins. Observation of a Rapidly Pulsating Radio Source. *Nature*, 217:709–713, February 1968.

[HKWE03] T. H. Hankins, J. S. Kern, J. C. Weatherall, and J. A. Eilek. Nanosecond radio bursts from strong plasma turbulence in the Crab pulsar. *Nature*, 422:141–143, March 2003.

[HL06] A. K. Harding and D. Lai. Physics of strongly magnetized neutron stars. *Reports on Progress in Physics*, 69:2631–2708, September 2006.

[Jar05] C. H. Jaroschek. *Critical Kinetic Plasma Processes In Astrophysics*. PhD thesis, Ludwigs-Maximilians-Universität München, 2005.

[JLK01] A. Jessner, H. Lesch, and T. Kunzl. Charge Densities above Pulsar Polar Caps. *ApJ*, 547:959–966, February 2001.

[JLK02] A. Jessner, H. Lesch, and T. Kunzl. Natural Limits for Currents in Charge Separated Pulsar Magnetospheres. In W. Becker, H. Lesch, and J. Trümper, editors, *Neutron Stars, Pulsars, and Supernova Remnants*, page 209, 2002.

[KKHC12] C. Kalapotharakos, D. Kazanas, A. Harding, and I. Contopoulos. Toward a Realistic Pulsar Magnetosphere. *ApJ*, 749:2, April 2012.

[KLO$^+$06] M. Kramer, A. G. Lyne, J. T. O'Brien, C. A. Jordan, and D. R. Lorimer. A Periodically Active Pulsar Giving Insight into Magnetospheric Physics. *Science*, 312:549–551, April 2006.

[Kra95] M. Kramer. *High Frequency Observations Of Pulsars*. PhD thesis, Max-Planck-Institut für Radioastronomie, December 1995.

[KW09] M. Kramer and N. Wex. TOPICAL REVIEW: The double pulsar system: a unique laboratory for gravity. *Classical and Quantum Gravity*, 26(7):073001, April 2009.

[LM92] Q. Luo and D. B. Melrose. Coherent curvature emission and radio pulsars. *MNRAS*, 258:616–620, October 1992.

[Mel78a] D. B. Melrose. Amplified linear acceleration emission applied to pulsars. *ApJ*, 225:557–573, October 1978.

[Mel78b] D. B. Melrose. Amplified linear acceleration emission applied to pulsars. *ApJ*, 225:557–573, October 1978.

[MG99] D. B. Melrose and M. E. Gedalin. Relativistic Plasma Emission and Pulsar Radio Emission: A Critique. *ApJ*, 521:351–361, August 1999.

[MHTH05] R. N. Manchester, G. B. Hobbs, A. Teoh, and M. Hobbs. ATNF Pulsar Catalog (Manchester+, 2005). *VizieR Online Data Catalog*, 7245:0, August 2005.

[Mos11] N. Moschüring. Simulation of radiation generated in boost frames. Master's thesis, LMU, 2011.

[MTW73] C. Misner, K.S. Thorne, and J.A. Wheeler. *Gravitation*. Freeman, 1973.

[NIS06] NIST. http://en.wikipedia.org/wiki/file:clock_accurcy.jpg, 2006.

[NU96] NASA and UIT. *Crab Nebula.* Astronomy Picture Of The Day, September 1996.

[NW94] K. Nishikawa and M. Wakatani. *Plasma Physics.* Springer, 1994.

[Rit93] H. Ritter. lecture notes on Pulsarastronomie, 1993.

[RK10] B. Reville and J. G. Kirk. Linear Acceleration Emission in Pulsar Magnetospheres. *ApJ*, 715:186–193, May 2010.

[Ruh] H. Ruhl. *Classical Particle Simulations With The PSC Code.*

[Sch02] R. Schopper. *Zur Dynamik relativistischer Teilchen in astrophysikalischen Plasmen.* PhD thesis, LMU, 2002.

[Stu71] P. A. Sturrock. A Model of Pulsars. *ApJ*, 164:529, March 1971.

[Yee66] K. Yee. Numerical solution of initial boundary value problems involving maxwell's equations in isotropic media. *Antennas and Propagation, IEEE Transactions on*, 14(3):302 –307, may 1966.

Acknowledgments...

...bzw Danksagung. Ich möchte mich bei einigen Personen bedanken, Allen voran Hartmut Ruhl, der mir schon zu Anfang meines Masterstudiums nicht nur einen Platz zum Arbeiten gegeben hat, sondern auch die Gelegenheit, am Lehrstuhl aktiv teilzunehmen und viel zu lernen. Auch ein größerer Themenwechsel brachte der Betreuung wie dem Vertrauen keinen Abbruch. Egal wie schwer oder trivial die Fragen waren, stets bekam ich kompetente und geduldige Antworten.
Dann möchte ich mich natürlich für das Thema selbst und die zahlreichen Stunden intensiver Betreuung bei Harald Lesch bedanken. Immer zur Stelle, wenn Not am Mann war, hätte ich mir keine angenehmere Arbeitsathmosphäre wünschen können. Betreuung kann nicht besser gemacht werden.
Ich bedanke mich auch bei Patrick Böhl, meinem Bürokollegen für die fruchtbaren Diskussionen an der Tafel, die mich vor dem ein oder anderen Fehlern bewahrt haben. Die Gespräche abseits der Tafel waren nicht weniger unterhaltend.
Für schnelle und kompetente Auskünfte über die Interna des PSC-Codes bedanke ich mich bei Karl-Ulrich Bamberg, Nils Moschüring und Fabian Deutschmann. Für die dann folgenden langen Diskussionen ebenso.
Ich danke Axel Jeßner und Michael Kramer für die Gelegenheit, meine Arbeit auch am Max-Planck-Institut für Radioastronomie in Bonn vorzustellen und für einige "Last-Minute"-Diskussionen ohne die die Arbeit wohl nicht komplett gewesen wäre.
Da auch ich der Thermodynamik unterliege und eine Arbeit geringere Entropie als die Umgebung aufweist, muss die Differenz notwendigerweise über mein Wirken in der Umwelt gelandet sein. Nicht zuletzt deshalb bedanke ich mich bei meiner Frau Katharina dafür, mein Gedankendurcheinander in Ordnung gebracht zu haben, und dafür, dass wir, trotz der aufregenden Zeiten, in denen wir stecken, die notwendige Ruhe, Muße und Zufriedenheit immer wieder finden.
Schließlich möchte ich mich bei meinen Eltern für die Unterstützung, nicht nur monetärer Art, bedanken, sondern auch die kleinen Dinge haben geholfen, mich in Gleichgewicht zu bringen, wie die Restauration meines Mountainbikes.
Euch Allen vielen vielen Dank.

Selbstständigkeitserklärung

Ich versichere, diese Arbeit selbstständig angefertigt zu haben, und dazu nur die angegebenen Quellen und Hilfsmittel verwendet zu haben.

München, den 7. August 2012